ELSEVIER

Contents lists available at ScienceDirect

Ocean Engineering

journal homepage: www.elsevier.com/locate/oceaneng



Research paper

Adaptive signal regime for identifying transient shifts: A novel approach toward fault diagnosis in wind turbine systems

Peng Chen a,b,*, Yuhao Wua, Shuai Fanc, Changbo Hed, Yaqiang Jine,f, Junyu Qig, Chengning Zhouh

- ^a College of Engineering, Shantou University, Shantou, 515063, Guangdong, China
- ^b Key Laboratory of Intelligent Manufacturing Technology, Ministry of Education, Shantou, 515063, Guangdong, China
- ^c School of Mechanical and Electrical Engineering, Chengdu University of Technology, Chengdu, 610059, Sichuan, China
- d College of Electrical Engineering and Automation, Anhui University, Hefei, 230601, China
- e School of Qilu Transportation, Shandong University, Jinan, 250061, Shandong, China
- f Qingdao Mingserve Tech, Qingdao, 266041, Shandong, China
- g Electronics & Drives, Reutlingen University, Reutlingen, 72762, Germany
- h Nuclear Power Institute of China, Chengdu, 610213, Sichuan, China

ARTICLE INFO

Keywords: Wind turbine Bearings Fault diagnosis Impulsive noise Signal processing Prognostics and health management

ABSTRACT

In real-world applications, the diagnostic efficiency of wind turbine systems, particularly rolling bearings, is significantly impaired by variable operating conditions such as fluctuating rotational speeds and varying loads, along with environmental disturbances including transient and non-Gaussian noises. These disturbances mask damage indicators, creating substantial challenges in accurate fault detection. Traditional diagnostic methods are often inadequate due to their sensitivity to noise and inability to identify failure signatures within multivariate random transient noise environments. To address these challenges in wind turbine fault diagnosis, this research introduces an adaptive signal processing regime with three key innovations: an adaptive signal tracking mechanism featuring real-time transient shift identification, a Dynamic Markov Transition Frequency with Adaptive Peak Rates (DMTF-APR) model for enhanced abnormality detection, and a Multi-Period Weighted Average Framework (MPWAF) that mitigates transient interference noise through the identification and replacement of anomalous signal fragments using periodic characteristics and weighted averages. Experimental validation with real-world wind turbine farm data demonstrates the framework's superior fault diagnosis performance, particularly in scenarios with complex non-Gaussian or transient noise interference, achieving significant improvements in detection accuracy and reliability compared to conventional methods.

1. Introduction

Wind turbines (WTs) are sophisticated electromechanical systems whose reliable operation depends critically on the health of their transmission chain components, particularly bearings (Du et al., 2024; Zhang et al., 2025; Huang et al., 2021). Despite their crucial role, these bearings operate under challenging conditions that include not only environmental stressors but also variable operational states such as fluctuating speeds and loads, making fault diagnosis particularly complex. The presence of transient and non-Gaussian noise further complicates the detection of incipient faults, as these disturbances can effectively mask early damage indicators. While conventional fault diagnosis methods have been widely implemented, their effectiveness is often compromised in real-world applications due to their sensitivity to noise and inability to

identify failure signatures within multivariate random transient noise environments (Xin et al., 2024). This challenge has created an urgent need for more robust and adaptive diagnostic approaches that can maintain accuracy under variable operating conditions.

The fault detection and diagnostics (FDD) for wind turbine systems has evolved through several complementary methodologies, including signal processing-based methods (Chen et al., 2024b; Jin et al., 2023), Machine Learning (ML) methods (Chen et al., 2020; Yao et al., 2024), and model-based approaches (Zemali et al., 2023). Among these, vibration signal analysis has emerged as a particularly effective approach, offering systematic identification of deterioration indicators through various analytical domains—including time domain (Chen et al., 2019; Panagiotopoulos et al., 2023), frequency domain (Zhao et al., 2024), time-frequency domain (Liu et al., 2023), and statistical analysis

E-mail address: pengchen@alu.uestc.edu.cn, dr.pengchen@foxmail.com (P. Chen).

^{*} Corresponding author.

Ocean Engineering 325 (2025) 120798

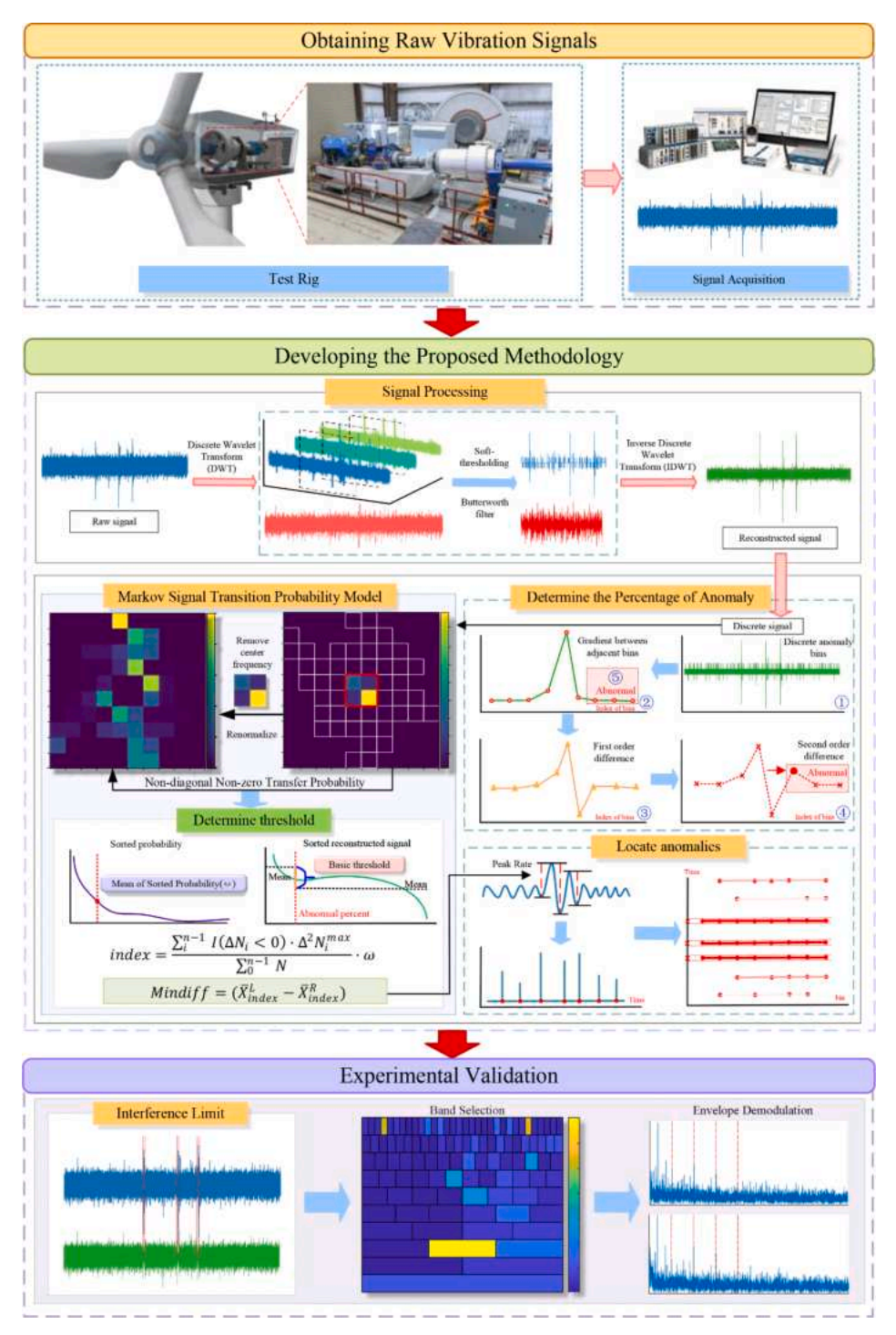


Fig. 1. The framework of the proposed Dynamic Markov Transition Frequency with Adaptive Peak Rates (DMTF-APR).

(Chen et al., 2024b; Kaewniam et al., 2022; Chen et al., 2025). This methodology proves especially valuable when extensive datasets are unavailable, as it relies primarily on physical understanding and established engineering principles. Contemporary deep learning approaches, including CNNs (Chen et al., 2021), ResNets (Chen et al., 2023b), and Transformers (Maldonado-Correa et al., 2024; Chen et al., 2024a), complement these traditional methods by uncovering complex nonlinear relationships in vibration signals, although they typically require substantial datasets and computational resources.

In the complex operational environment of wind farms, vibrationbased diagnosis faces significant challenges due to multiple interference sources. Various localized defects, such as pitting and surface cracks, produce distinctive vibration signatures that manifest as characteristic fault frequencies. However, these signatures are often masked by non-Gaussian noise, transient disturbances, and impulsive variations from various sources, including non-targeted mechanical elements, auxiliary systems, and environmental factors. The time-varying nature of these interferences, coupled with their non-stationary characteristics, makes it particularly challenging to isolate specific fault frequencies associated with bearing components.

Recent research has attempted to address these challenges through various innovative approaches. Traditional methods using Spectral Kurtosis (SK) (Antoni, 2006) have been enhanced through developments such as $CYCBD_{\beta}$ (Peng et al., 2023), which improves robustness against

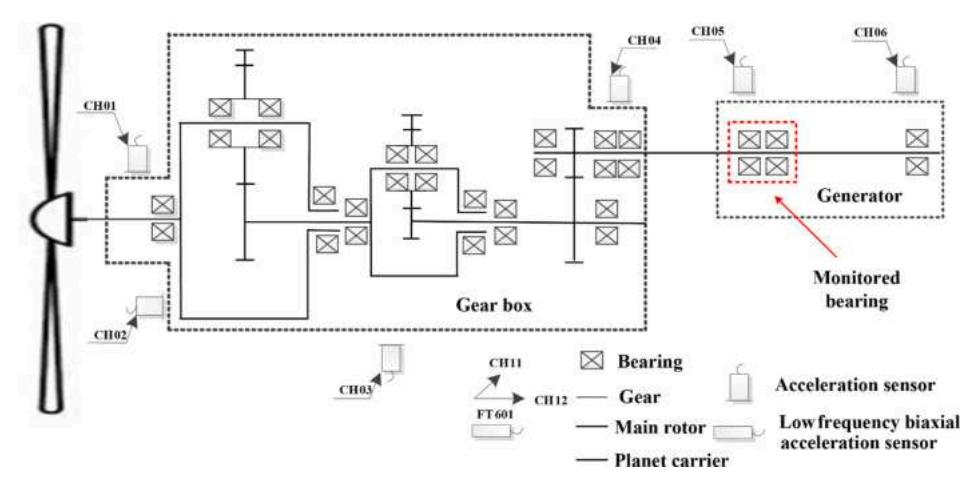


Fig. 2. Schematic representation of the wind turbine system structure.



Fig. 3. Installation locations of vibration accelerometers on the wind turbine generator, mounted horizontally and vertically (Chen et al., 2021).

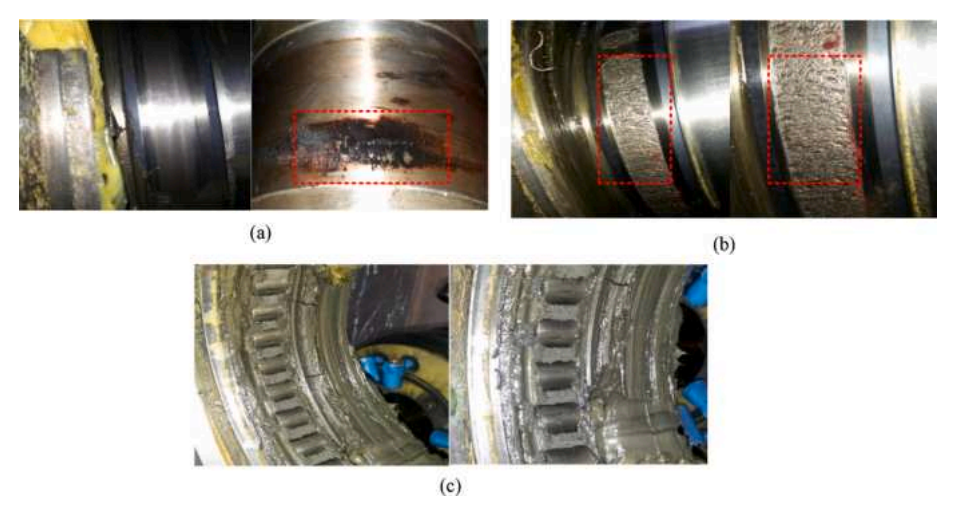


Fig. 4. Defects on the worn inner surface of rolling bearings, highlighted by red dotted areas indicating inner race failures. (a) Inner race electrical corrosion failure of the bearing; (b) Worn inner surface of the bearing inner race; (c) Roller of the wind turbine bearing.

non-Gaussian noise, and the ARKurtogram method (Peng et al., 2024), which enables automated and noise-resistant bearing fault detection. Other notable advances include the Cyclogram (Li et al., 2023) for improved frequency band selection, the STAKgram method (Jia et al., 2024), the Ensefgram (Wang et al., 2024), the SEACKgram (Wang et al., 2025), and the IESFSIOgram (Sun et al., 2025) for handling complex interference. However, these approaches still demonstrate considerable sensitivity to operational parameters and often rely on complex post-processing strategies.

To address the inherent complexities and limitations of previous fault diagnosis techniques, which have demonstrated considerable sen-

sitivity to operational parameters and frequently relied upon complex post-processing signal strategies to manage interference, this research presents a novel methodological framework. Traditional approaches have proven insufficiently robust, particularly in scenarios characterized by multivariate random pulse noise, thus necessitating the development of an innovative strategy that can effectively address these challenges. The proposed methodology in this paper proposes a sophisticated approach designed to systematically suppress transient interference noise directly associated with non-stationary vibration signals. Specifically, this method exploits the fundamental properties of non-stationary signals observed in mechanical vibrations when subjected to transient noise

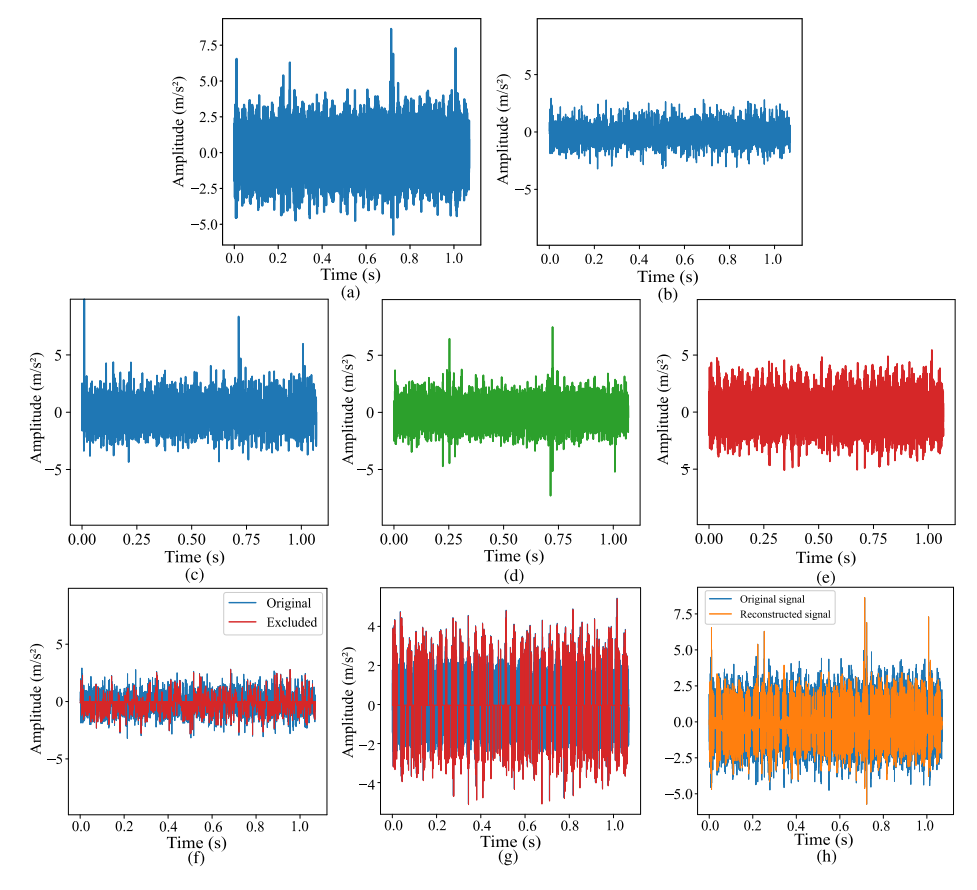


Fig. 5. Comparative analysis of signal processing stages in case I: (a) Raw signal, (b) Level 1approximation coefficient, (c) Detail coefficient (level 1), (d) Detail coefficient (level 2), (e) Detail coefficient (level 3), (f) Low-pass filtered approximation coefficients, (g) Threshold-processed detail coefficients and (h) Comparative visualization of original and reconstructed signals.

interference. Through this strategic approach, the method endeavors to enhance the robustness of the demodulation process against transient noise, thereby facilitating a more precise and reliable selection of demodulation bands.

To accomplish these objectives, the methodology encompasses several key components. Initially, it introduces an adaptive signal regime specifically designed for identifying and tracking transient shifts in the signal through a novel adaptive signal tracking mechanism, which incorporates real-time transient shift identification and dynamic threshold adjustment. This regime systematically addresses the challenges of non-stationary vibration signals by exploiting their fundamental properties when subjected to transient noise interference. The mechanism's adaptive nature ensures robust detection of signal variations even under complex operating conditions, enhancing the overall demodulation process. Subsequently, it establishes a comprehensive signal transition model termed Dynamic Markov Transition Frequency with Adaptive Peak Rates (DMTF-APR). This model integrates state transition matrices with adaptive peak rate analysis, providing precise tracking and identification of abnormal signal components. The model's transition matrix serves as an advanced temporal monitor, continuously evaluating signal state evolution and facilitating accurate abnormality detection. Finally, it proposes a Multi-Period Weighted Average Framework (MPWAF) for anomalous signal fragment mitigation that identifies and replaces anomalous signal fragments using periodic characteristics and weighted averages. This framework effectively mitigates transient interference noise, enabling more precise and reliable selection of demodulation bands. The framework's effectiveness has been validated through extensive experimental studies using real-world wind turbine farm data, demonstrating superior performance in fault diagnosis, particularly in challenging scenarios involving non-Gaussian or transient noise interference.

The principal contributions of this research can be summarized as follows:

- A novel adaptive signal tracking mechanism is proposed, which incorporates real-time transient shift identification and dynamic threshold adjustment, enabling robust detection of signal variations in complex operating conditions.
- An innovative Dynamic Markov Transition Frequency with Adaptive Peak Rates (DMTF-APR) model is developed, which integrates sophisticated state transition matrices and adaptive peak rate analysis, facilitating precise abnormality detection and temporal monitoring of signal characteristics.
- 3. A Multi-Period Weighted Average Framework (MPWAF) identifies and replaces anomalous signal fragments using periodic characteristics and weighted averages, effectively mitigating transient interference noise to enable more precise and reliable selection of demodulation bands.
- 4. The effectiveness of the proposed method is validated through comprehensive experimental studies using real-world wind turbine farm data, demonstrating superior performance in fault diagnosis compared to existing approaches, particularly in scenarios with non-Gaussian or transient noise interference.

The comprehensive research framework is systematically structured and organized as follows: Initially, Section 2 presents a thorough review and critical analysis of the primary metrics employed in the identification of signal status transformation, while establishing the theoretical foundation for the subsequent methodological development.

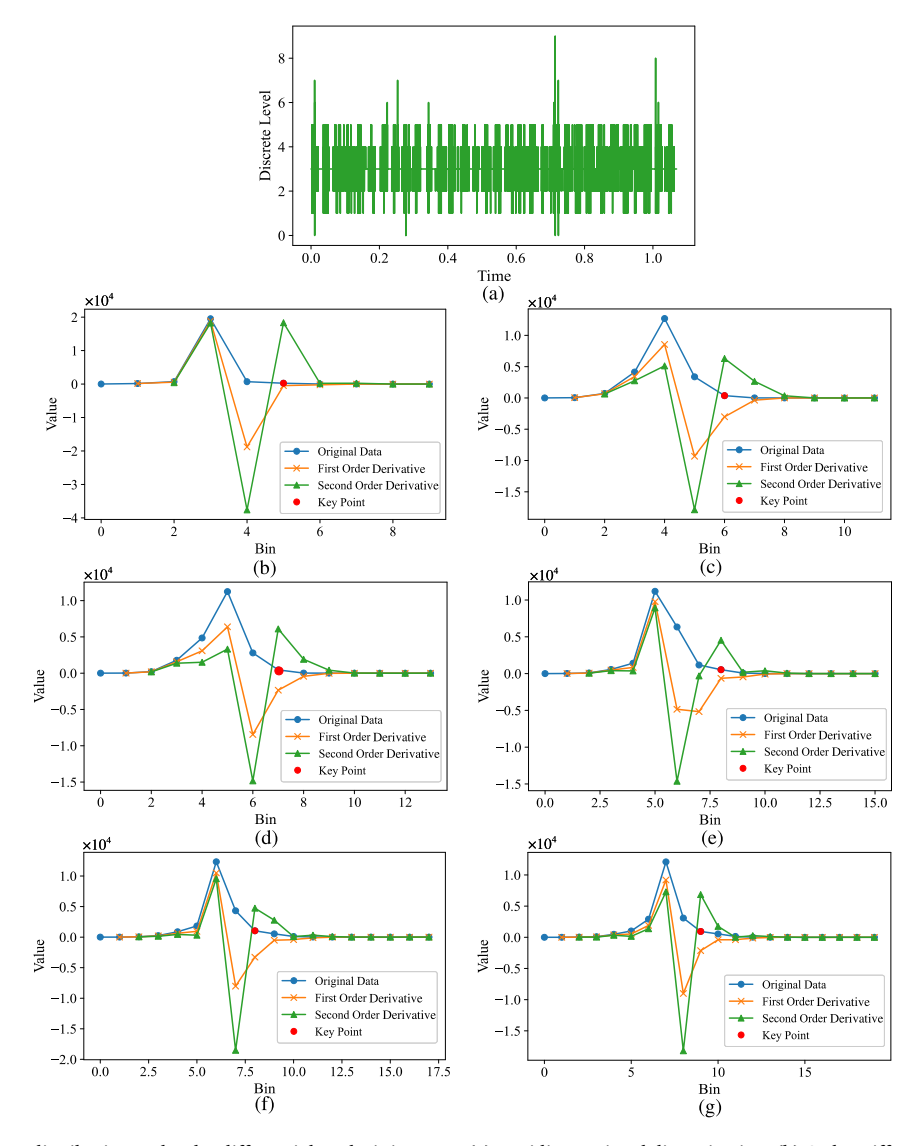


Fig. 6. Multi-scale signal state distribution and order differential analysis in case I: (a) Equidistant signal discretization, (b) Order Differential Analysis (bin = 10), (c) Order Differential Analysis (bin = 12), (d) Order Differential Analysis (bin = 14), (e) Order Differential Analysis (bin = 16), (f) Order Differential Analysis (bin = 18), (g) Order Differential Analysis (bin = 20).

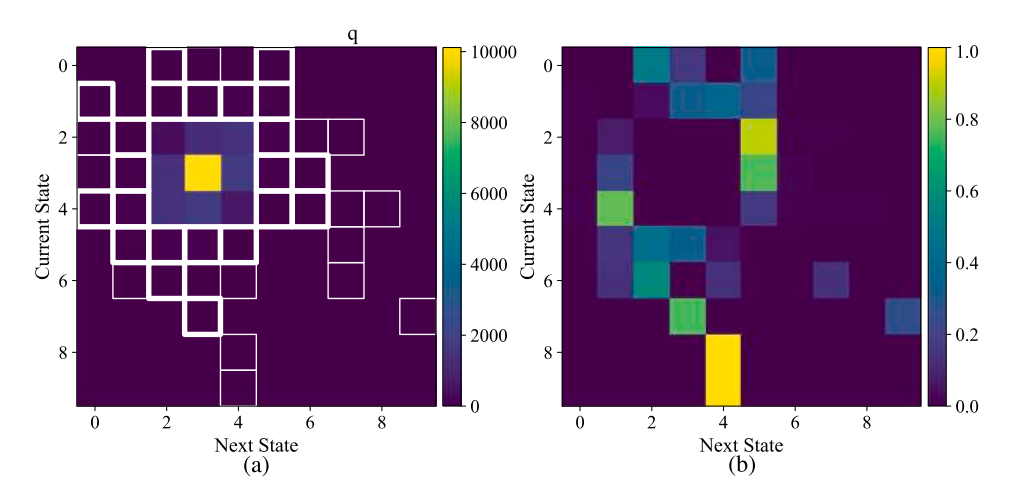


Fig. 7. Markov signal transition analysis in case I: (a) Markov signal frequencies heat-map, (b) Scaled Markov signal probability heat-map.

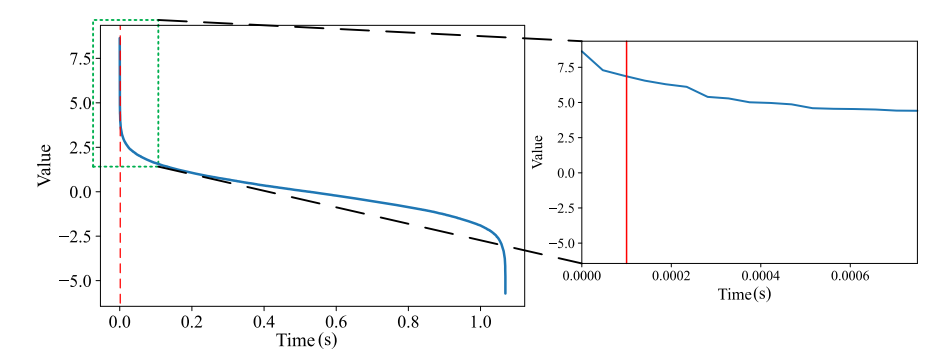


Fig. 8. Quantitative analysis of signal anomaly in case I: Determination of the signal anomaly index.

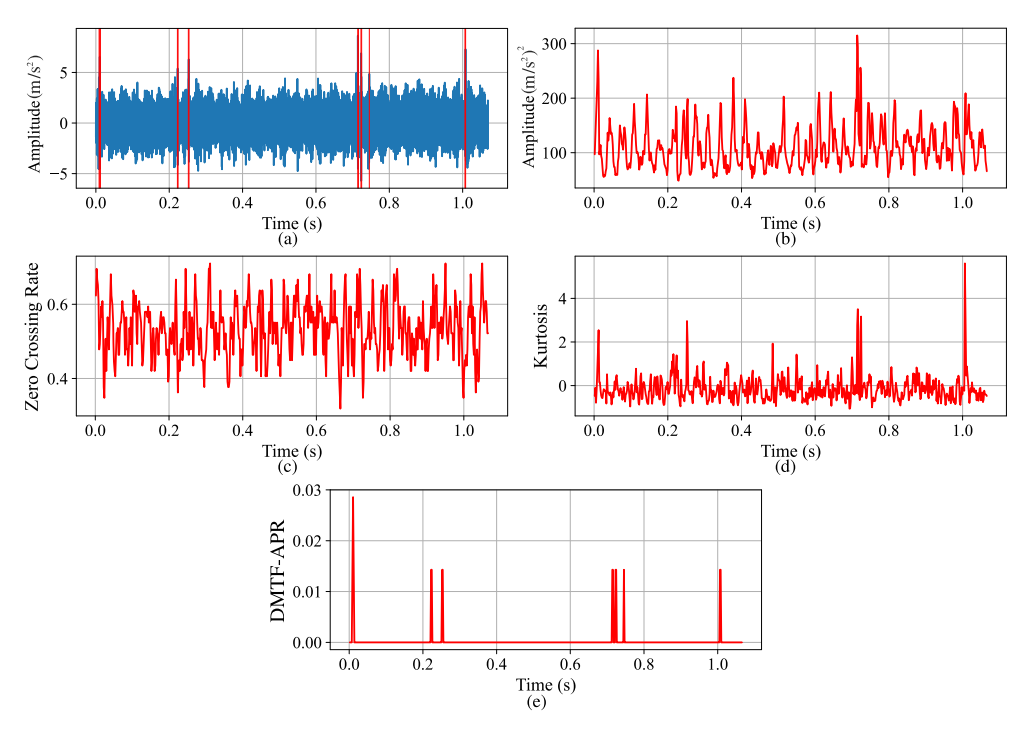


Fig. 9. Comparative analysis of indicators in case I: (a) Raw Signal, (b) STE, (c) STZCR, (d) STK, and (e) DMTF-APR.

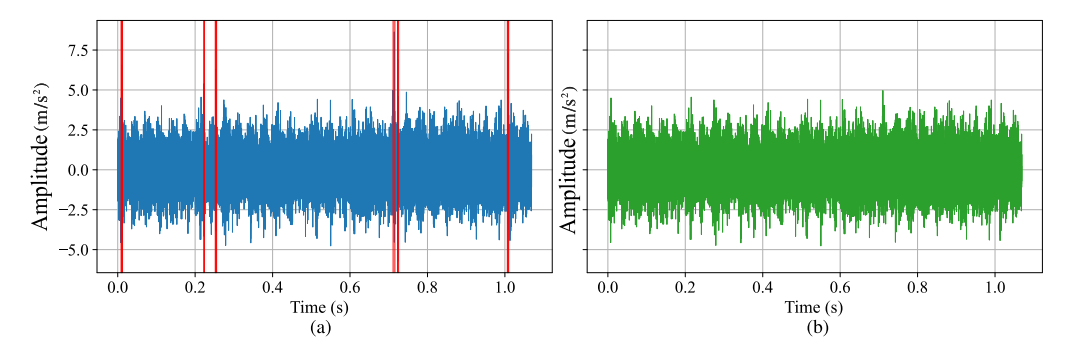


Fig. 10. Comparative analysis in Case I: (a) Weak interference signal characteristics, (b) Post-Interference substitution signal profile.

Following this foundational overview, Section 3 introduces and elaborates on the proposed Dynamic Markov Transition Frequency with Adaptive Peak Rates (DMTF-APR) model, delineating its mathematical formulation and operational principles. To demonstrate the practical efficacy and robustness of the proposed methodology, two distinct case studies are presented in Section 4. The first case study employs validation datasets acquired from a real-world wind turbine farm to evaluate the methodology's effectiveness under authentic operational conditions. Subsequently, the second case study uti-

lizes laboratory-generated datasets to further validate the methodology's performance under general operating conditions, particularly focusing on scenarios where transient noise interference introduces additional complexity to the measurement data. The research investigation concludes in Section 5, where the key findings are synthesized and critically analyzed, accompanied by comprehensive insights into the broader implications of the proposed method for fault diagnosis applications, as well as potential directions for future research endeavors.

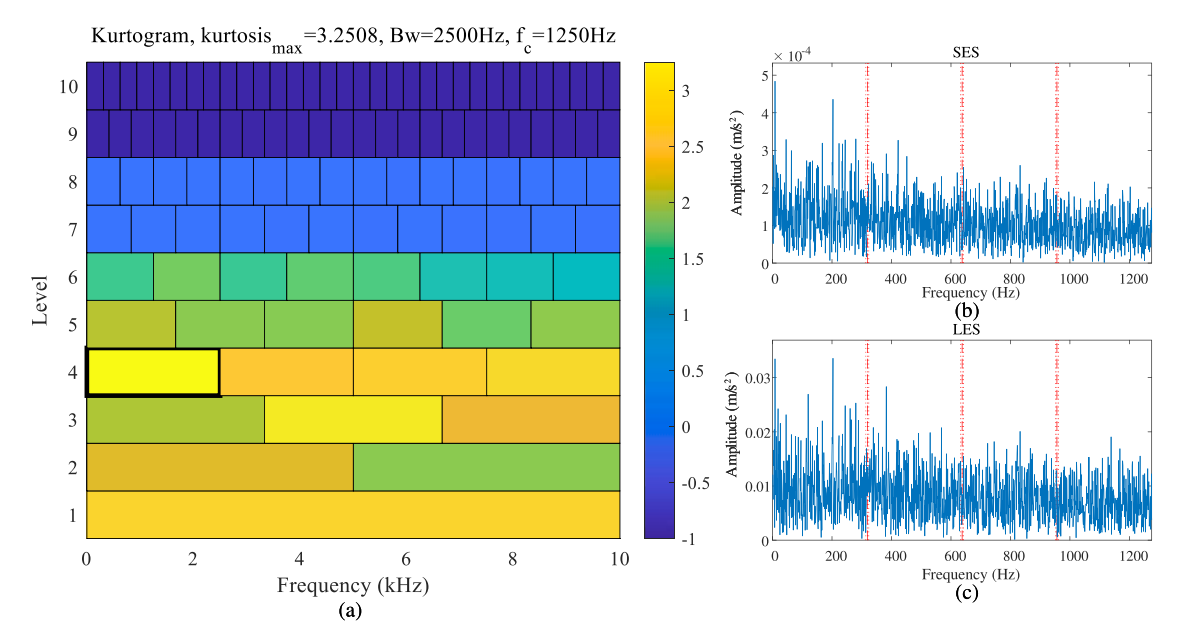


Fig. 11. Raw signal affected by external transient noise interference in Case I: (a) Demodulation band determination via Fast-Kurtogram, (b) Squared envelope spectrum, (c) Logarithmic scale envelope spectral analysis.

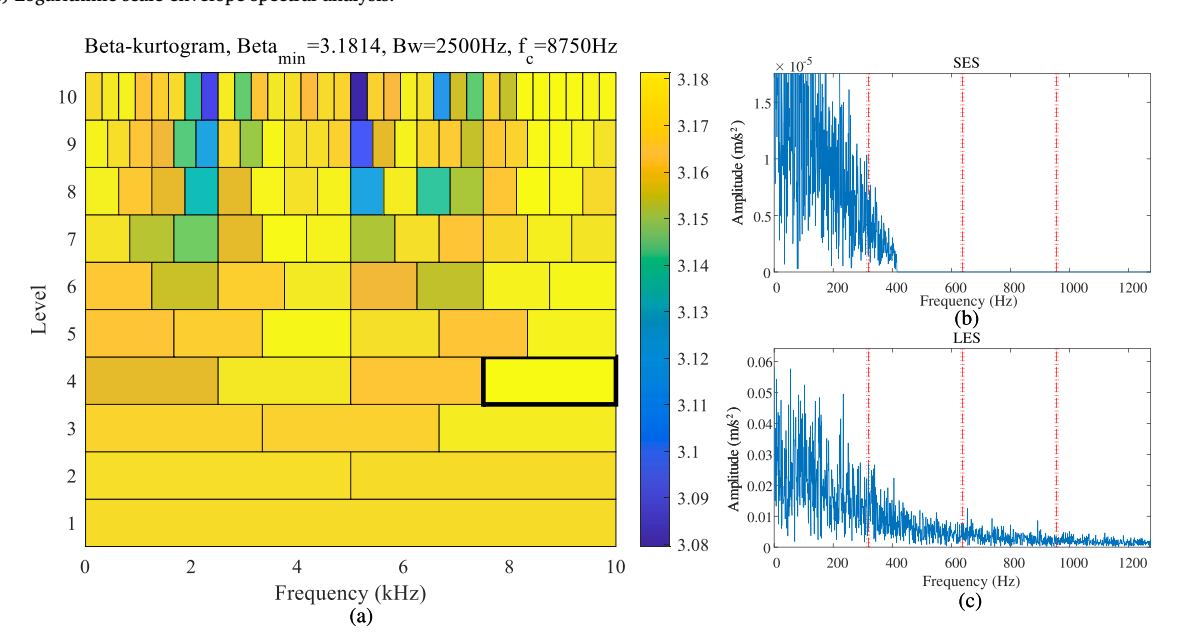


Fig. 12. Raw signal affected by external transient noise interference in Case I: (a) Demodulation band determination via Beta-Kurtogram, (b) Squared envelope spectrum, (c) Logarithmic scale envelope spectral analysis.

2. Related theory

In this section, the primary metric employed for the detection of signal transformations is revisited, and it should be further analyzed. Established methodologies, such as Short-Time Energy (STE) (Schirmer and Mporas, 2020), Short-Time Kurtosis (STK) (Alimi and Awodele, 2022), and Short-Time Zero Crossing Rate (STZCR) (Schirmer and Mporas, 2020; Chen et al., 2023a), have proven to be critical in the identification of anomalous signal patterns. These methodologies offer insights into various aspects, including peak ratios, energy deployment, and the frequency of zero crossings, thereby contributing to the field.

When analyzing real-world discrete signals, these signals are often represented as a time series, symbolically denoted as $[x_n]$, where n spans from the initial point of 1 to the termination point N. The signal can be calculated using the following equation:

$$x_f[m] = x[m+f \cdot h] \cdot w[m] \tag{1}$$

where m represents the time index, f denotes the frame index, and h specifies the duration of the sliding window. The application of a window function, typically a rectangular one labeled w, ensures even weighting across all frame samples, leading to more accurate signal calculations

Subsequently, the procedure incorporates the identification of local maxima within each segment of the signal encapsulated by the sliding window. A peak is recognized when a data point's amplitude exceeds those of its immediate neighbors. This principle is succinctly represented in the following formula:

$$x[m] - x[m-1] > 0,$$

 $x[m+1] - x[m] \le 0$ (2)

The identification of local peaks indicative of signal alterations necessitates an assessment that accounts for the magnitude of eachpeak.

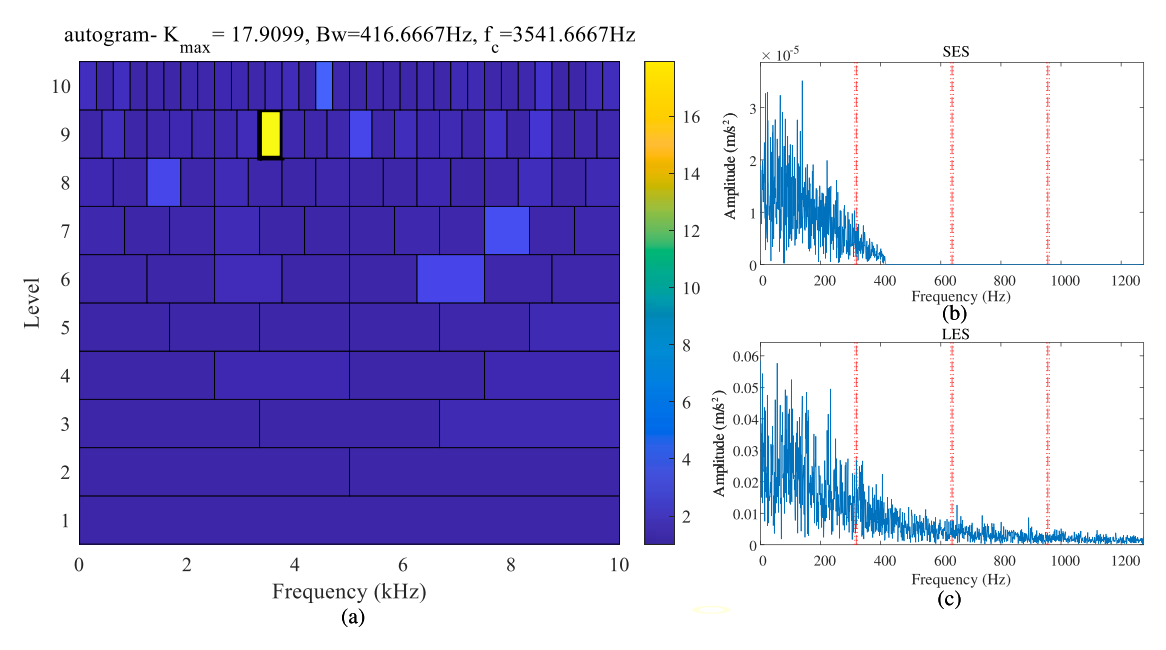


Fig. 13. Raw signal affected by external transient noise interference in Case I: (a) Demodulation band determination via Autogram, (b) Squared envelope spectrum, (c) Logarithmic scale envelope spectral analysis.

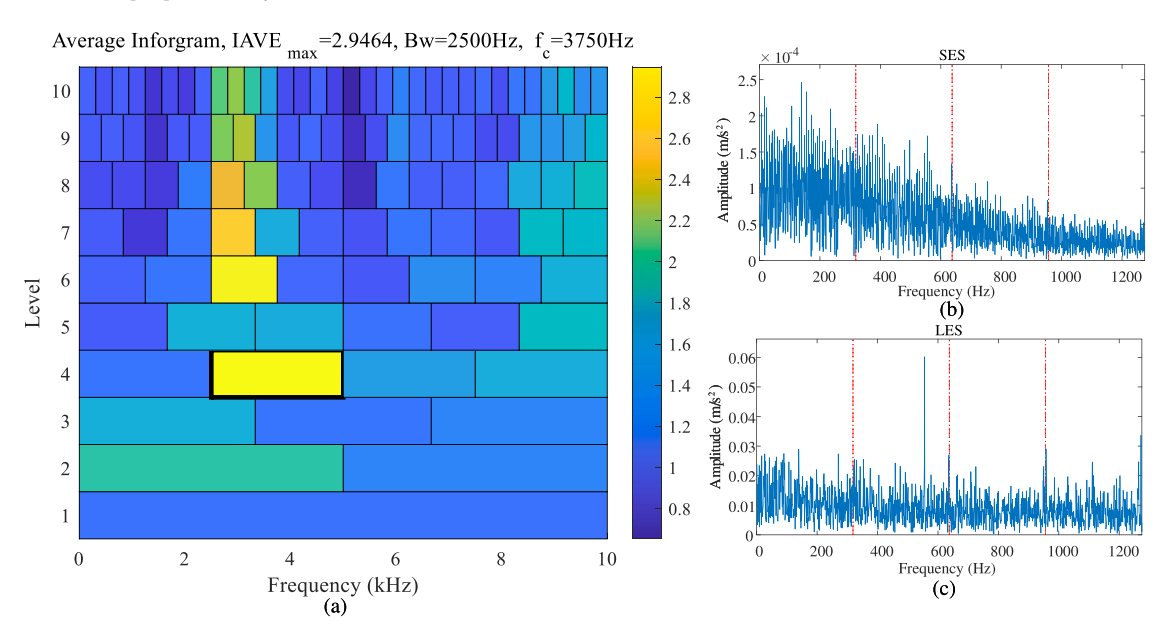


Fig. 14. Raw signal affected by external transient noise interference in Case I: (a) Demodulation band determination via Infogram, (b) Squared envelope spectrum, (c) Logarithmic scale envelope spectral analysis..

Relying solely on amplitude, as is common in some prevalent techniques (Schirmer and Mporas, 2020; Alimi and Awodele, 2022), risks obscuring the signal's intrinsic variations due to noise interference. By introducing a defined threshold, m_d , the process of detecting local maxima amidst variable and intermittent noise interference is refined. This refinement facilitates consistent observation of signal transitions and enhances precision in identifying discrepancies.

$$\begin{split} x[m] - x[m-1] &> m_d \\ x[m+1] - x[m] &\leq m_d \end{split} \tag{3}$$

After the filtering process, local peaks that meet specific criteria, denoted as N_p , are pinpointed within a designated sliding window. Following this, the ratio of N_p to the total number of samples in the windowis

accurately calculated, which defines the Short-Term Local Peak Rate (STLPR):

$$STLPR = \frac{N_p}{M} \tag{4}$$

where M represents the length of the window function.

The evaluation of local maxima through the sliding window framework is facilitated by Eq. (4), which accurately measures the aggregation of outlier points within the signal's active window.

3. The proposed methodology of dynamic Markov transition frequency with adaptive peak rates (DMTF-APR)

As previously discussed, the accuracy of anomaly detection is significantly influenced by the careful selection of a conditional local peak

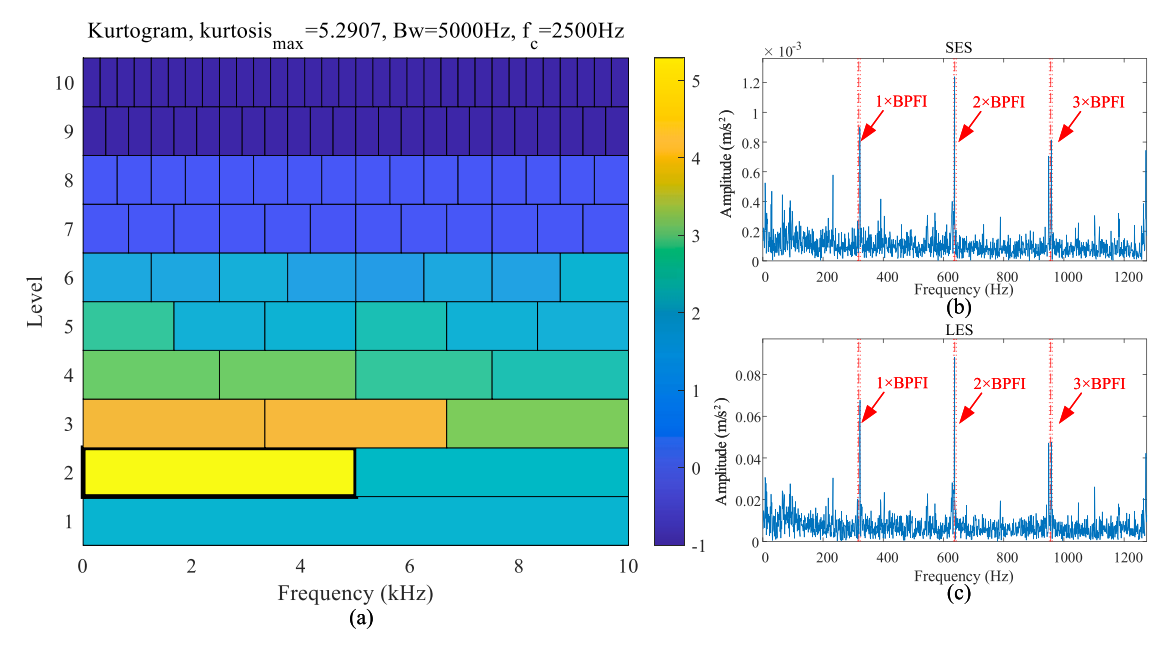


Fig. 15. Case I: (a) Fast-Kurtogram-assisted demodulation band selection for post-interference substitution and amplitude limitation, (b) Squared envelope spectrum, (c) Logarithmic scale envelope spectral analysis.

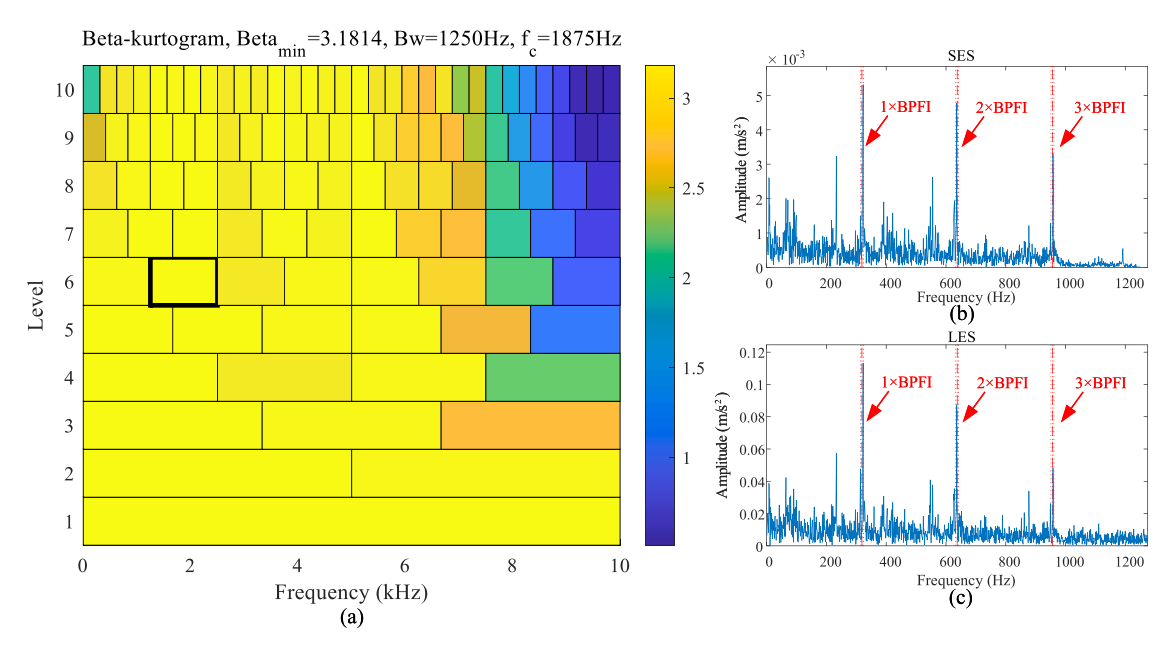


Fig. 16. Case I: (a) Beta-Kurtogram-assisted demodulation band selection for post-interference substitution and amplitude limitation, (b) Squared envelope spectrum, (c)Logarithmic scale envelope spectral analysis.

threshold, denoted as m_d . Traditional methods frequently exhibit vulnerability to non-Gaussian noise, and they encounter substantial challenges in adapting to the variability inherent in signal properties. In response to these issues, Dynamic Markov Transition Frequency with Adaptive Peak Rates (DMTF-APR) method has been proposed. This approach involves a systematic sequence of steps designed to automatically adjust the threshold, thereby eliminating the need for complex manual settings and substantially enhancing the system's adaptability to intricate signal environments. The methodology encompasses several principal components: initial signal processing, Markov modeling to monitor temporal state changes, dynamic peak-rate analysis of discrete transfer frequencies, adaptive adjustment of the anomaly percentage, and the determination of robust exception boundaries for multiple bins. The framework of this proposed method is depicted in the flowchart below, see in Fig. 1.

3.1. Wavelet-based signal decomposition and Markov state initialization

Initially, the Discrete Wavelet Transform (DWT) is utilized due to its attributes of smoothness and superior frequency and time resolution, providing an effective means for the initial analysis of signals and the identification of transients and anomalies. By decomposing a vibration signal x(t), the DWT produces two primary coefficients: the approximation coefficient $c\,A_{j,k}$, which captures general trends, and the detail coefficient $c\,D_{j,k}$, which highlights minute variations.

$$x(t) = \sum_{k=-\infty}^{+\infty} cA_{j,k} \phi_{j,k}(t) + \sum_{k=-\infty}^{+\infty} cD_{j,k} \psi_{j,k}(t)$$
 (5)

where j represents the scale factor of the wavelet, while k determines its shift factor, thereby establishing the central position. The function $\phi_{j,k}$ and $\psi_{j,k}$ correspond to the wavelet and scale functions, respectively.

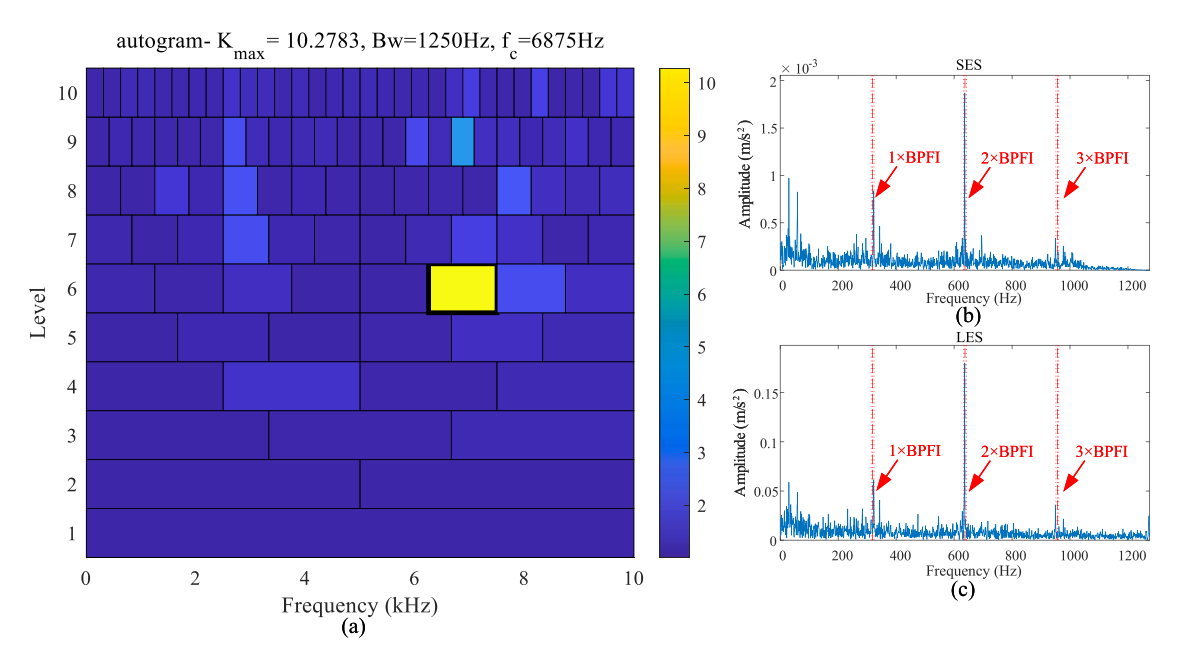


Fig. 17. Case I: (a) Autogram-assisted demodulation band selection for post-interference substitution and amplitude limitation, (b) Squared envelope spectrum, (c) Logarithmic scale envelope spectral analysis.

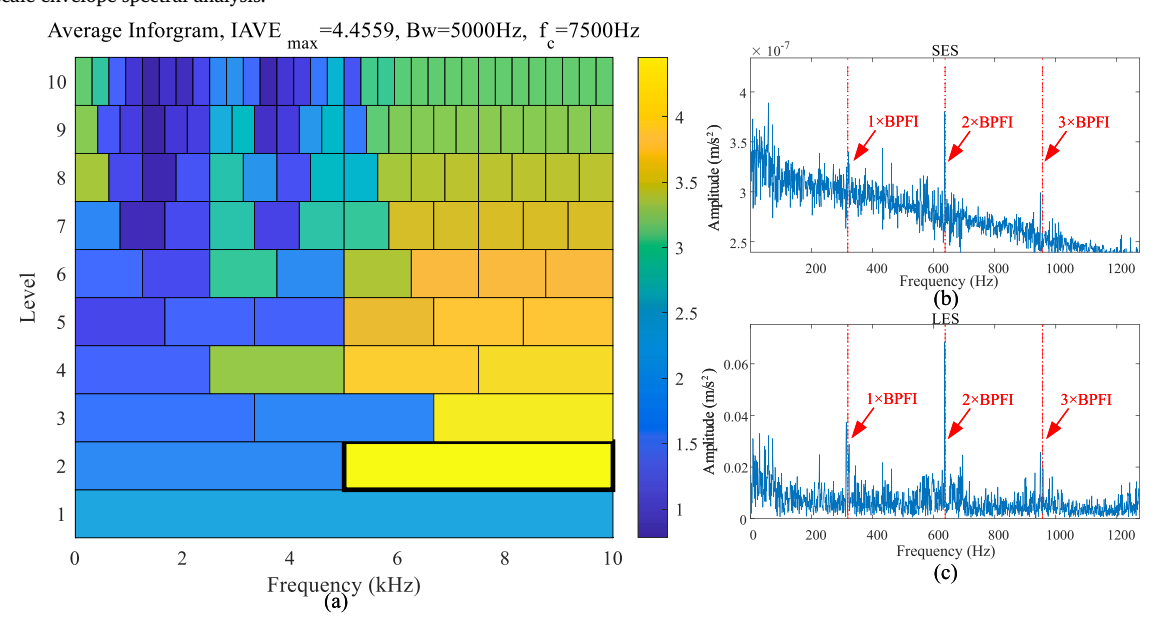


Fig. 18. Case I: (a) Infogram-assisted demodulation band selection for post-interference substitution and amplitude limitation, (b) Squared envelope spectrum, (c) Logarithmic scale envelope spectral analysis.

During the discrete wavelet transform decomposition, higher-level approximation and finer detail coefficients are progressively acquired at each stage. This enables the preservation and retrieval of signal characteristics across different frequency ranges and levels until the target decomposition level is reached. This process can be mathematically represented by the following expressions:

$$cA_{j,k} = \sum_{n} h[n - 2k]x_{j-1,n}$$

$$cD_{j,k} = \sum_{n} g[n - 2k]x_{j-1,n}$$
(6)

where h[n] and g[n] serve as the low-pass and high-pass filters, respectively. The variable $x_{j-1,n}$ represents the low-frequency component of the current approximation coefficient, reflecting the global and long-term trends of the entire signal.

Subsequently, the approximation and detail coefficients undergo further processing through thresholding and filtering operations. The processed approximation coefficients, denoted as cA', are derived from the application of a Butterworth filter. This procedure is mathematically articulated as follows:

$$cA'_{n} = \sum_{i=0}^{M} b_{i} \cdot cA_{n-i} - \sum_{j=1}^{N} a_{j} \cdot cA'_{n-j}$$
(7)

The Butterworth filter has feed-forward coefficients b_i and feed-back coefficients a_i . In this case, the index j begins at 1 and a_0 is set to 1 for normalization. Then, soft-thresholding is applied to the detail coefficients cD' at each decomposition level to effectively reduce noise:

$$cD_i' = \begin{cases} \operatorname{sgn}\left(cD_i\right)\left(\mid cD_i\mid -\varepsilon\right) & \mid cD_i\mid \geq \varepsilon \\ 0 & \mid cD_i\mid <\varepsilon \end{cases} \tag{8}$$

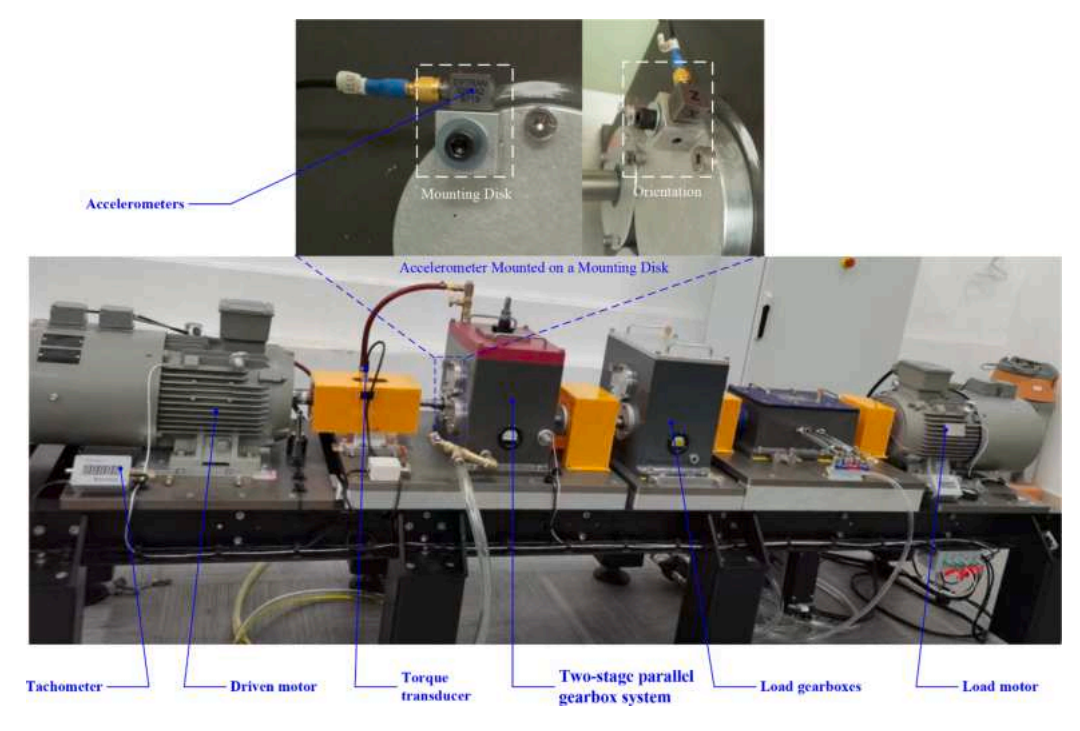


Fig. 19. Schematic representation of the experimental apparatus for gear transmission system analysis with detailed component identification.

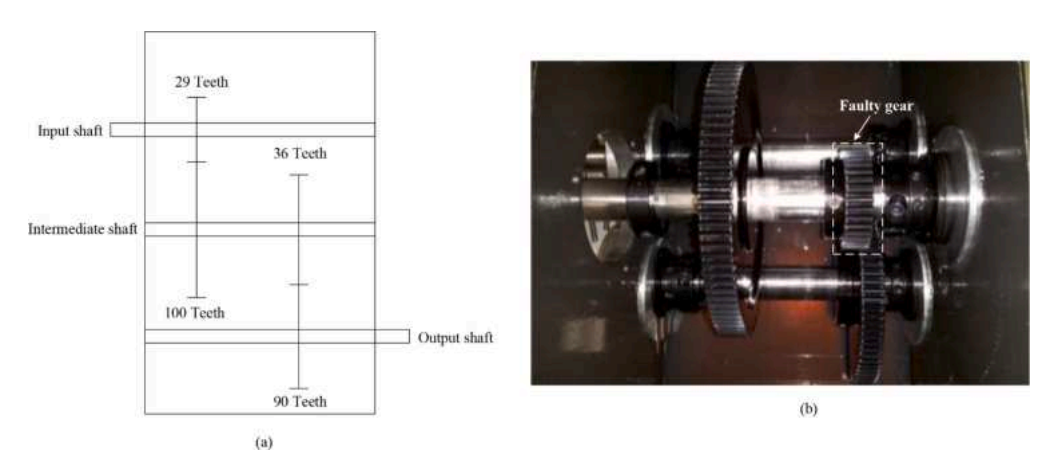


Fig. 20. Structural configuration of the gear system: (a) Detailed gear meshing mechanism, (b) Internal architecture of parallel gearbox system with fault location indication.

The threshold value ε is a specified proportion of the maximum value of cD_i , articulated as follows:

$$\varepsilon = e \cdot \max\left(cD_i\right) \tag{9}$$

After the coefficients are processed, they are recombined via the Inverse Discrete Wavelet Transform (IDWT) to form a new signal sequence. This reconstructed sequence is crucial for retrieving important signal information and eliminating noise and other disturbances. The reconstruction is represented mathematically as:

$$\hat{x}(t) = \sum_{j=-\infty}^{\infty} \left(c A'_{j,k} \phi_{j,k}(t) + \sum_{k=-\infty}^{\infty} c D'_{j,k} \psi_{j,k}(t) \right)$$
 (10)

The reconstruction process is essential, as it aids in identifying peaks that deviate from the mean of the original signal, as specified by the following condition:

$$\Pi = \{i | x_i(t) > \tau \lor x_i(t) < -\tau, i \in \{1, \dots, |n|\}\}$$
(11)

where τ represents the mean of the original signal. Consequently, the peak retrieval in the reconstructed signal is expressed as:

$$\hat{x}_i'(t) = \begin{cases} x_i(t), & \text{if } i \in \Pi \\ \hat{x}_i(t), & \text{if } i \notin \Pi \end{cases}$$
 (12)

Lastly, a Markov model is employed to statistically capture and describe transition patterns among states in the reconstructed signal, reflecting the principle that a system's future state is solely dependent on its current state, irrespective of prior states. This is captured by the following first-order Markov model formula:

$$P(x_i \mid x_{i-1}, x_{i-2}, \dots, x_1) = P(x_i \mid x_{i-1})$$
(13)

The above expression indicates that the probability of transitioning to the subsequent state, x_i , is entirely contingent upon the current state, x_{i-1} .

In Markov chains, each step can involve either a transition from one state to another state or the retention of the current state. This transition process is determined by a predefined probability distribution. The determination of the current state relies solely upon the most recent pre-

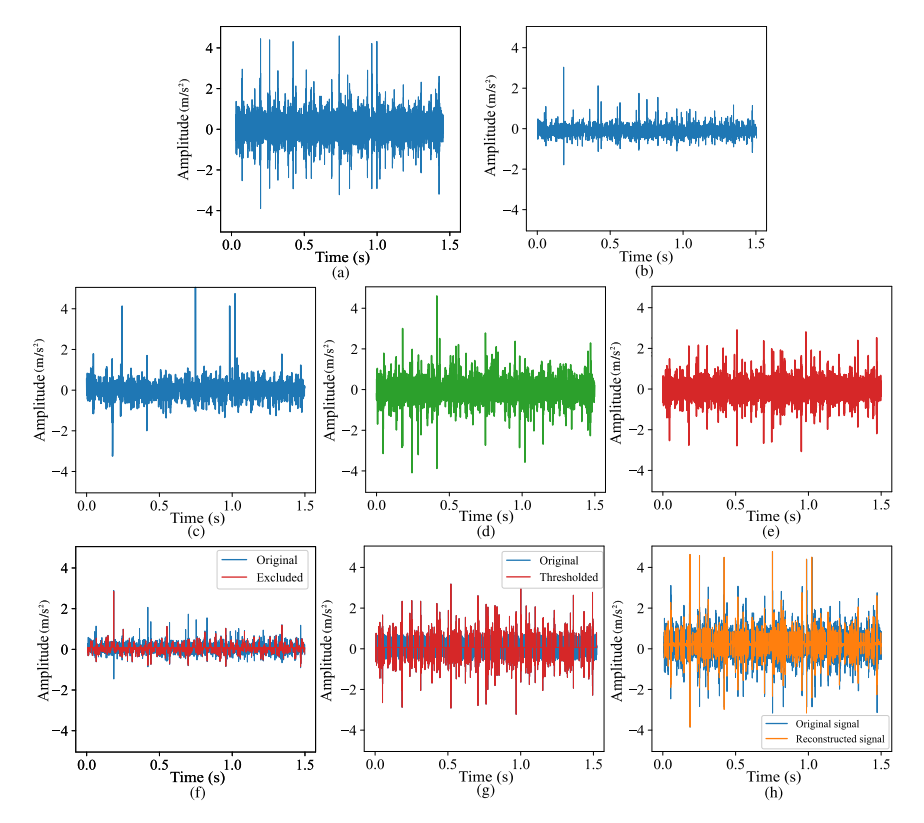


Fig. 21. Case II: (a) Raw signal, (b) Level 1 approximation coefficient, (c) Detail coefficient (level 1), (d) Detail coefficient (level 2), (e) Detail coefficient (level 3), (f) Low-pass filtered approximation coefficients, (g) Thresholded detail coefficients and (g) Raw and reconstructed Signals.

ceding state, embodying the renowned Markov property, which posits that the future state depends only on the present state and is independent of the sequence of events that preceded it. This specific dependency is quantified through a transition probability matrix. This matrix enumerates the conditional probabilities of transitioning between all conceivable pairs of states. For a system comprising n states, this matrix provides an exhaustive overview of n^2 potential transition scenarios. The matrix is formulated using a defined approach as follows:

$$M_{TPM} = \begin{bmatrix} p_{11} & p_{12} & \cdots & p_{1j} & \cdots \\ p_{21} & p_{22} & \cdots & p_{1j} & \cdots \\ \vdots & \vdots & & \vdots & & \vdots \\ p_{i1} & p_{i2} & \cdots & p_{ij} & \cdots \\ \vdots & \vdots & \vdots & \vdots & & \vdots \end{bmatrix}$$
(14)

3.2. Dynamic Markov transition frequency with adaptive peak rates

Prior to establishing a Markov model, signal discretization is refined through equal-interval segmentation. This approach allocates the amplitudes of the cleaned signals, which are reconstructed via wavelet transformation, to fixed intervals, denoted by j. Each partition corresponds to a discrete level of signal amplitude, which is then mapped onto a discrete set of state spaces S_i , effectively serving as the nodes within the Markov model. Through this method, complex signals are translated into a streamlined discrete format. This transformation, delineated by Eq. (10), allows the Markov model to track interval sequences rather than precise amplitude values, as indicated by Eq. (15). Consequently, this enhances the ability to differentiate between typical and atypical states, as transitions between these discrete states reflect the intrinsic laws of the signal. This, in turn, facilitates the construction of Markov models that effectively capture the time series and the inherent randomness of signals.

$$S_{i} = \begin{cases} j, & x_{n}[i] \in S_{j} \\ j, & x_{n}[i] = \max(x_{n}), j = n_{bin} - 1 \end{cases}$$
 (15)

The initial signal is then segmented into states denoted as S_i . In this specific scenario, the signal is divided into 10 distinct intervals, represented as $n_{bin} = 10$.

$$S_{j} = \left[\min\left(x_{n}\right) + (j-1) \cdot \Delta L, \min\left(x_{n}\right) + j \cdot \Delta L\right]$$

$$\Delta L = \frac{\max\left(x_{n}\right) - \min\left(x_{n}\right)}{n_{\text{bin}}}$$
(16)

where ΔL signifies the consistent division used for discretizing signals, and n_{bin} defines the level of detail and clarity in the portrayal of discrete states within the analysis of Markov models.

Subsequently, the occurrence counts of signal transitions in each bin are tallied. Building upon this, the first derivative is calculated to observe the trend of signal transition counts as a function of bin variation. Under typical circumstances, given the amplitude distribution of discrete signals, most regular signals cluster around the central bin values, resulting in a bell-shaped trend that rises and declines gradually. When the first derivative reaches a minimum value, it marks the point where the signal transition count peaks before declining, signifying a reduction in the proportion of normalcy. Further analysis through the second derivative helps identify areas where the first derivative's rate of change of begins to slow, indicating a deceleration in the decline of signal transition counts. The bin corresponding to the second local maximum of the second order derivative marks the onset of this slowing trend. Bins following this point are characterized as exceptionally high-value intervals and flagged as anomalous, exemplifying significant deviations from the norm in signal transition patterns. This distribution-based method provides a statistical mechanism to identify and pinpoint unusual behaviors within the signal. Additionally, the ratio of these abnormal bins' frequency to the total frequency serves as the baseline for quantifying the percentage of signal anomaly. This process is shown in the formula

$$index = \frac{\sum_{i}^{n-1} I(\Delta N_{S_{i}} < 0) \cdot \Delta^{2} N_{S_{i}}^{max}}{\sum_{i}^{n-1} N} \cdot \omega$$
 (17)

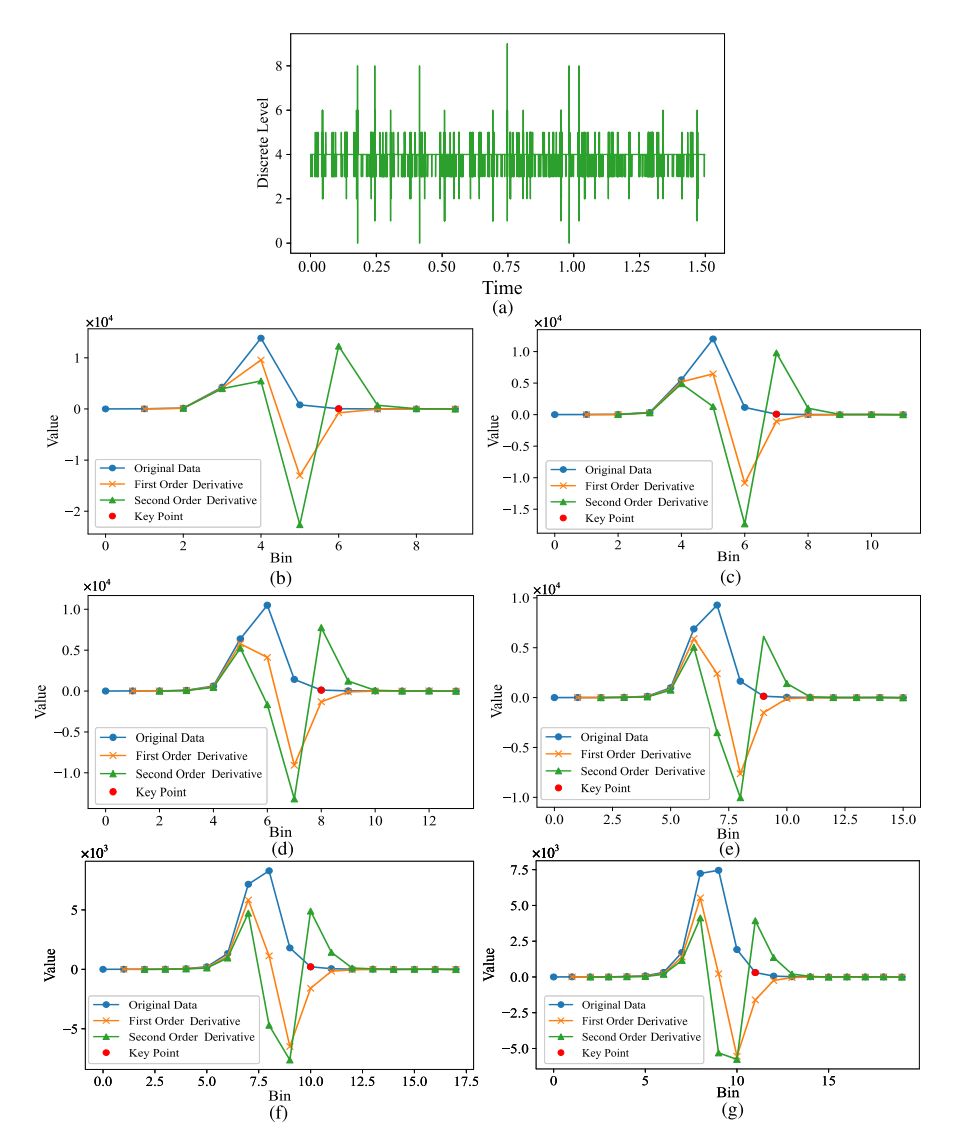


Fig. 22. Case II: Order differential analysis with (a) Equidistant signal discretization, and analysis results using different bin numbers: (b) bin = 10, (c) bin = 12, (d) bin = 14, (e) bin = 16, (f) bin = 18, (g) bin = 20.

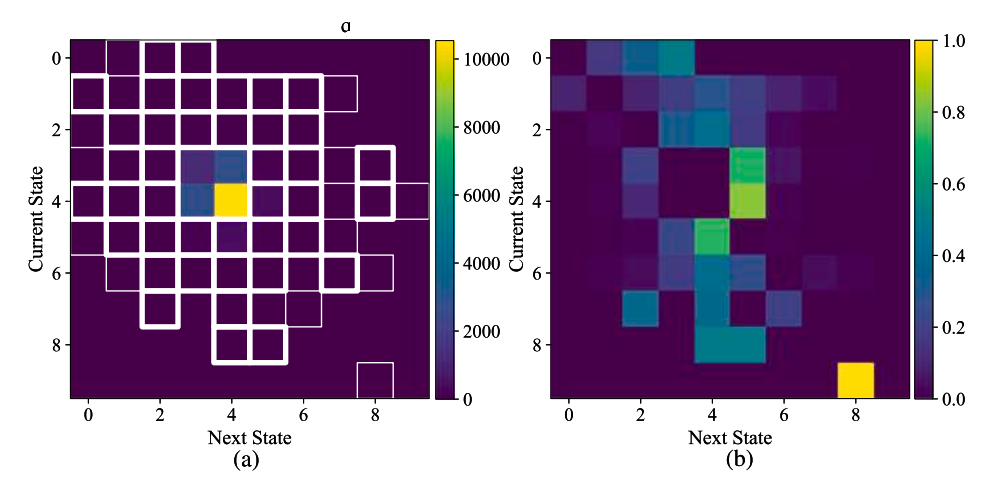


Fig. 23. Case II: (a) Markov signal frequencies heat-map, (b) Scaled Markov signal probability heat-map.

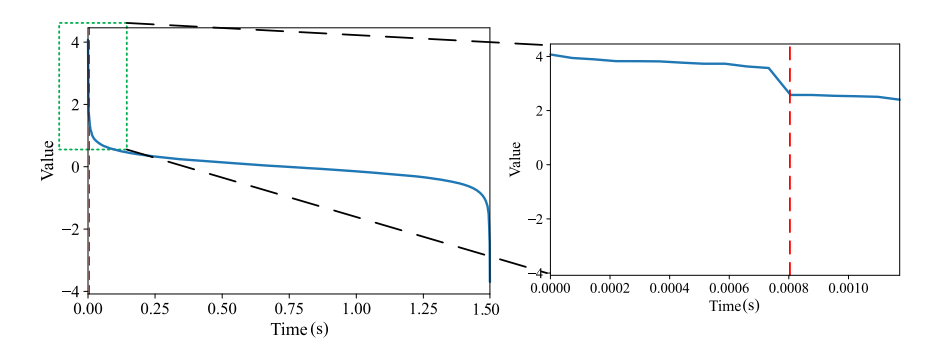


Fig. 24. Case II: Determination of the signal anomaly index.

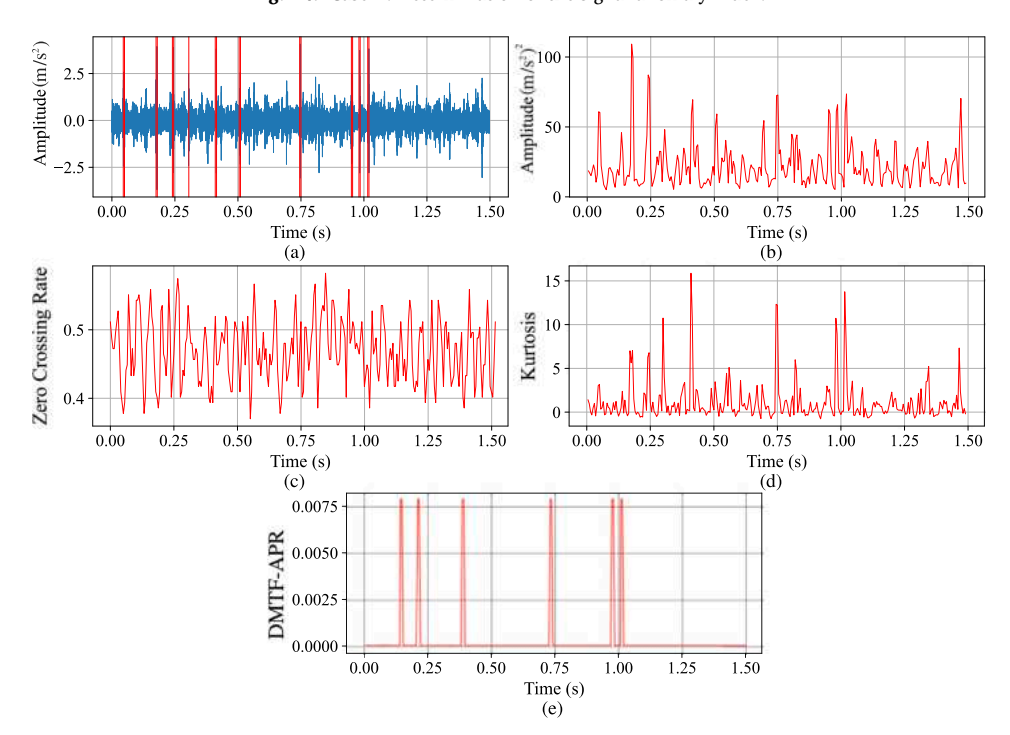


Fig. 25. Case II: (a) Raw Signal, (b) STE, (c) STZCR, (d) STK, and (e) DMTF-APR.

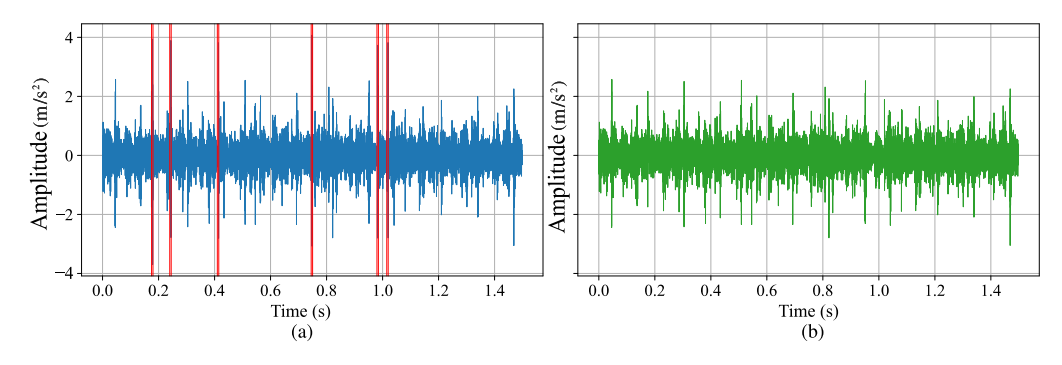


Fig. 26. Case II: (a) Signals with random interference, (b) Vibration signal with Interference substitution.

where I denotes the indicator function, Δ represents the first derivative, while Δ^2 stands for the second derivative, and ω is an adjustment weight factor, provided in subsequent calculations.

Next, the signal amplitude is reordered in descending order. During this process, the previously defined percentage baseline index is used as a dividing line, further dividing the signal into two segments. Among them, the high-value region on the left side of the dividing line is defined as an abnormal amplitude, while the part on the right is recognized as normal amplitude. When determining a signal's peak rate, a key aspect is to set an appropriate amplitude threshold, and choosing the amplitude

height difference as the threshold is a reasonable approach. Therefore, the average of the signal areas on the left and right of the baseline is calculated and subtracted to establish a threshold, as illustrated in the following formula:

$$\hat{M}_d = \left(\bar{X}_{index}^L - \bar{X}_{index}^R\right) \tag{18}$$

where X^L_{index} and X^R_{index} represent the mean of the amplitudes on the left and right sides of the baseline in descending order, respectively.

In observing the process of determining the baseline, it becomes evident that manual fine-tuning to derive threshold values often results in

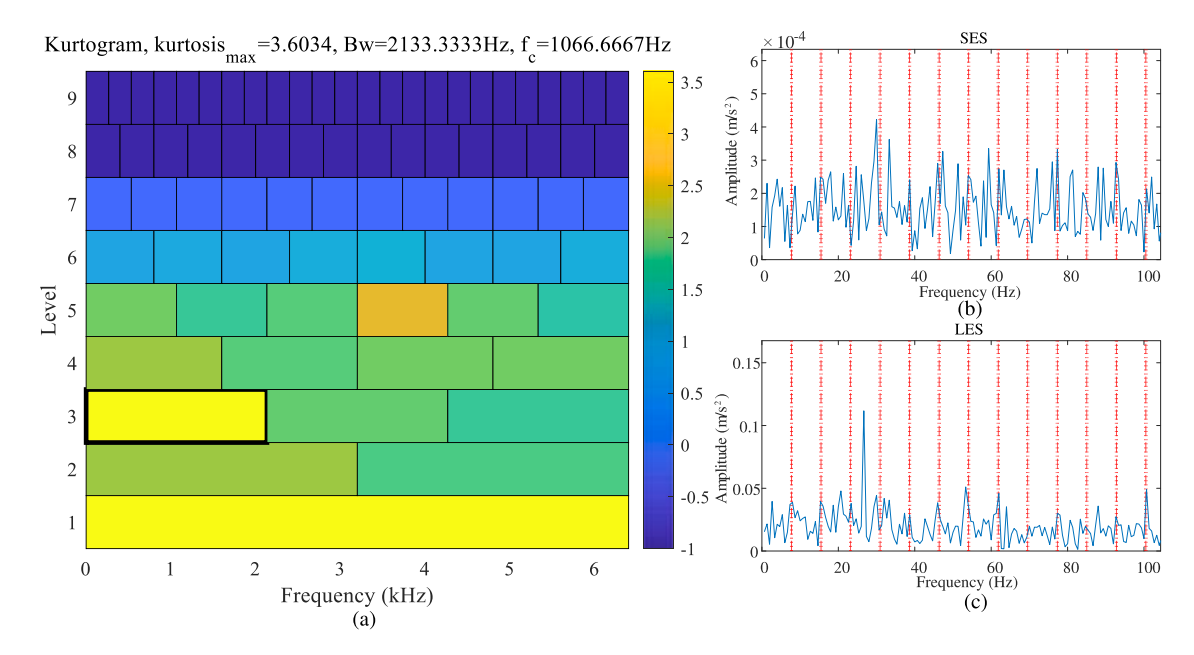


Fig. 27. Raw signal affected by external transient noise interference in Case II: (a) Demodulation band determination via Fast-Kurtogram, (b) Squared envelope spectrum, (c) Envelope spectrum in logarithmic scale.

deviations. This deviation is marked by a lower threshold as the baseline shifts to the right (i.e., as the index increases), leading to the identification of more peaks and a higher chance of false positives. To address this issue, an adjustment weighting factor is introduced to shift the baseline to the left (i.e., decrease the index).

Once the state sequence is obtained, a matrix is constructed using the Markov Transition Matrix (MTM) to determine the frequency of transitions from one state to another. This matrix plots these transition frequencies, with each element denoted as A_{ii}^{MTM} .

$$A_{ij}^{MTM} = \sum_{0}^{n-1} \delta(S_n = i, S_{n+1} = j)$$
 (19)

where $\delta(x, y)$ represents the Kronecker Delta, which yields a value of 1 if x equals y and 0 in all other cases. N indicates the total number of states in the sequence S.

Subsequently, much like distinguishing between normal and abnormal baselines, it is imperative to identify and eliminate the frequencies of regular transitions within the Markov transition frequency matrix. This reconfiguration retains only the frequencies of distinctive transitions, effectively isolating atypical transfers from commonplace ones. The resulting matrix exclusively maps these specialized transitions, effectively filtering the data for enhanced specificity. This process is illustrated in the formula below:

$$\theta = \alpha \cdot \sum_{i=0}^{n-1} \sum_{i=0}^{n-1} A_{ij}^{MTM}$$
 (20)

$$A_{ij}^{MTM'} = \begin{cases} 0 & \text{if } i = j \text{ or } A_{ij}^{MTM} > \theta \\ A_{ij}^{MTM} & \text{if } i \neq j \text{ and } A_{ij}^{MTM} \leq \theta \end{cases}$$
 (21)

where α signifies the proportion of standard transition occurrences relative to the aggregate frequency, determined to be 0.1. θ refers to the determined normal transfer frequency.

The state matrix, denoted as M_{TPM} is normalized through the exclusion of standard elements. This process culminates in the emergence of a novel Markov transition matrix elements denoted by P_{ij} , which amplifies the prevalence of atypical transitions within the matrix. It intricately outlines the probability of shifting from any state i to a different

state j.

$$P_{ij} = \frac{A_{ij}^{MTM'}}{\sum_{j=0}^{n-1} A_{ij}^{MTM'} - \left(1 + A_{ij}^{\theta}\right)}$$
(22)

where the variable A^{θ}_{ij} refers to the count of regular transitioning elements in the specified row which exceed a threshold value, represented by θ .

Next, The transformation process involves unfolding the transition probability matrix M_{TPM} into a one-dimensional vector, represented as $F_{\rm sorted}$. Following this, every non-zero element within this vector is painstakingly singled out. These elements are then organized in a descending arrangement.

$$F_{\text{sorted}} = \text{sort}_{\text{desc}} \left(\left[P_{ij} \mid P_{ij} > 0, \ \forall (i,j) \in \Omega(M_{TPM}) \right] \right) \tag{23}$$

where $\Omega(M_{TPM})$ represents the indexes for all non-zero elements.

Building upon this, the mean of the sorted probabilities is determined, symbolizing the central tendency of anomalous transitions and reflecting the overall status of anomaly probabilities. This approach, when used in conjunction with the amplitude of anomalous signals placed on the left side of the sorted baseline, utilizes the mean of this probability matrix as the adjustment factor ω , enabling the formulation of a more robust Peak Rate (PR), as illustrated in the following formula:

$$PR = \frac{1}{M} \sum_{n=0}^{M-2} I\left((\Delta x_n > \hat{M}_d) \wedge (\Delta x_{n+1} > \hat{M}_d) \right)$$
 (24)

where I denotes the indicator function and Δx_n represents the value of $x_n - x_{n-1}$. This function assigns a value of 1 when the argument enclosed within it is positive and assigns a value of 0 otherwise.

Following a comprehensive analysis of the Dynamic Markov Transition Frequency with Adaptive Peak Rates (DMTF-APR) across the entirety of the signal spectrum, the calculated average values are systematically employed not only to establish a robust threshold for detecting abnormal boundaries but also to define an adaptive fault-tolerant window that enables the identification of previously overlooked anomalies. Subsequently, precise modifications are meticulously applied to specific segments of the original signal that correspond to these identified frames, particularly where amplitude spikes require regulation. This procedure

can be expressed through the following formula.

$$B = \left\{ g \mid PR[g] > \gamma \cdot \left(\frac{1}{G} \sum_{g=0}^{G-1} PR[g] \right) \right\}$$
 (25)

where B defining anomaly boundaries, γ as the average coefficient.

After identifying potential anomalous locations, a sieving mechanism is introduced to analyze anomalies across different bins. By aggregating results from multiple bins, calculating the frequency of occurrence for each location, and applying frequency distribution, the most likely anomaly positions are selected. This process ensures high robustness and accuracy by integrating information from multiple bins.

Due to the stiffness of the absence of anomalous fragments, the amplitude and frequency characteristics of the time series need to be considered. The highest amplitude of each frequency is calculated and the mean value is extracted, the first k frequencies with the highest amplitude are selected from these amplitudes, and finally, the corresponding period is calculated for each selected frequency, so as to capture the periodic characteristics of the signal more accurately, so as to make an effective time series replacement while preserving the basic characteristics of the signal. The process can be computed as follows.

$$p_i = \left\lceil \frac{T}{f_i} \right\rceil \quad \text{where} \quad \{f_1, \dots, f_k\} = \arg_{f_* \in \{1, \dots, \left\lfloor \frac{T}{2} \right\rfloor\}}$$
 (26)

 $Topk(Avg(|FFT(\hat{x}_{\epsilon})|))$

where Topk(Avg(|FFT(\hat{x}_t)|)) represents the k highest values selected from the averaged frequency amplitudes obtained through Fast Fourier Transform analysis.

Furthermore, the weight coefficient w_i for each epoch p_i must be determined. This weight is mathematically defined as the ratio of the ith frequency's amplitude to the cumulative sum of all selected frequency amplitudes. This normalization ensures that the sum of weights equals unity, thereby establishing a more robust foundation for subsequent weighted average calculations:

$$w_i = \frac{Amp(f_i)}{\sum_{j=1}^k Amp(f_j)}, \quad i \in \{1, 2, \dots, k\}$$
 (27)

where $Amp(\cdot)$ denotes the amplitude calculation operator.

For the purpose of anomalous fragment replacement, it is essential to compute the weighted average across multiple distinct periods. To facilitate this, we define the set $C_i(t)$ as the collection of non-missing value indices corresponding to time point t within each epoch p_i , expressed

$$C_{i}(t) = \left\{ (t - j) \bmod N \mid j = 0, 1, 2, \dots, \left\lfloor \frac{T}{p_{i}} \right\rfloor \right\}$$
such that $[(t - j) \bmod N]_{\text{missing}} = 0$ (28)

Through comprehensive analysis and iterative computations, the final prediction value is derived by systematically aggregating the weighted averages across all temporal periods, whereby the Multi-Period Weighted Average Framework (MPWAF), as formulated in (29). This framework not only identifies but also systematically replaces anomalous signal fragments by leveraging inherent periodic characteristics and optimized weighted averages. Consequently, the framework effectively mitigates transient interference noise, which in turn enables significantly more precise and reliable selection of demodulation bands for subsequent signal analysis.

$$y_{predict}^{n} = \sum_{i=1}^{k} w_{i} \cdot \frac{1}{|C_{i}(t)|} \sum_{j \in C_{i}(t)} \hat{x}_{t}[j], n \in (g \cdot M, g \cdot M + h), \forall g \in B$$
 (29)

This comprehensive methodological framework serves the dual purpose of effectively mitigating anomaly-induced distortions while preserving the signal's fundamental characteristics. The mathematical rigor employed in this approach ensures robust signal reconstruction while maintaining the integrity of essential temporal patterns and relationships within the data structure. The process is outlined in the pseudoalgorithm presented in Algorithm 1.

Algorithm 1 Dynamic Markov Transition Frequency with Adaptive Peak Rates (DMTF-APR).

Phase I: Multi-Resolution Wavelet Decomposition and Signal Reconstruction

Input: Original temporal vibration sequence: x(t)

- 1: Implementation of Discrete Wavelet Transform decomposition: $x(t) = \sum_{k=-\infty}^{+\infty} c A_{j,k} \phi_{j,k}(t) + \sum_{k=-\infty}^{+\infty} c D_{j,k} \psi_{j,k}(t) D$
- 2: Extraction of approximation and detail coefficients: $cA_{i,k}$ and $cD_{i,k}$
- 3: Application of adaptive filtering to $cA_{j,k}$ and soft thresholding to
- 4: Signal reconstruction via Inverse DWT:

$$\hat{x}(t) = \sum_{j=-\infty}^{\infty} \left(cA'_{j,k} \phi_{j,k}(t) + \sum_{k=-\infty}^{\infty} cD'_{j,k} \psi_{j,k}(t) \right)$$

Output: Processed signal $\hat{x}(t)$

Phase II: Dynamic Peak Rate Analysis and Threshold Optimization

Input: Reconstructed signal $\hat{x}(t)$

- 5: Implementation of uniform signal discretization
- 6: Computation of second-order derivatives and adaptive threshold:

: Computation of second-order define
$$index = \frac{\sum_{i=1}^{n-1} I(\Delta N_{S_i} < 0) \cdot \Delta^2 N_{S_i}^{\max}}{\sum_{i=1}^{n-1} N} \cdot \omega$$

- 7: Generation of Markov transition frequency matrix: MTM
- 8: Normalization of transition probability matrix: TPM
- 9: Estimation of optimal peak rate threshold:

$$\hat{M_d} = \left(\bar{X}^L_{index} - \bar{X}^R_{index}\right)$$

Output: Optimized threshold \hat{M}_d

Phase III: Statistical Validation and Signal Enhancement

Input: Derived threshold \hat{M}_d

10: Computation of temporal peak rate utilizing threshold:

$$PR = \frac{1}{M} \sum_{n=0}^{M-2} I((\Delta x_n > \hat{M}_d) \wedge (\Delta x_{n+1} > \hat{M}_d))$$

11: Definition of anomalous signal regions:

$$B = \left\{ g \mid PR[g] > \gamma \cdot \left(\frac{1}{G} \sum_{g=0}^{G-1} PR[g] \right) \right\}$$

12: Implementation of amplitude constraint for anomaly mitigation:
$$y_{predict}^n = \sum_{i=1}^g w_i \cdot \frac{1}{|C_i(t)|} \sum_{j \in C_i(t)} \hat{x}_t[j], n \in (g \cdot M, g \cdot M + h), \forall g \in B$$

Output: Enhanced signal $\hat{x}(t)$ with controlled interference

4. Experimental validation analysis

To rigorously evaluate and validate the effectiveness of the proposed methodology, two distinct case studies will be conducted. The first case study, detailed in Section 4.1, examines a real-world wind farm application, whereby the dataset has been systematically collected from an operational wind farm located in LU NAN, China. Furthermore, the second case study, presented in Section 4.2, involves an experimental test-rig of a gear transmission system, which serves to demonstrate the method's efficacy in gear fault diagnosis through controlled laboratory conditions. These complementary studies were specifically selected because they represent both field-based and laboratory-controlled environments, thus providing comprehensive validation across different operational contexts.

4.1. Case study I

4.1.1. Test rig and data acquisition

The proposed methodology for fault diagnosis in wind turbine systems, particularly focusing on generator bearing diagnostics, has been extensively validated through empirical vibration data collected from an operational wind farm situated in LU NAN, China. The primary subject of investigation is a doubly-fed induction generator (DFIG) wind turbine system, whose detailed configuration is illustrated in Fig. 2. This particular installation comprises an offshore 1.5-MW three-bladed horizontal P. Chen et al. Ocean Engineering 325 (2025) 120798

axis system, which represents a commonly deployed configuration in modern wind energy applications.

To enable comprehensive monitoring, twelve accelerometers were strategically positioned along various points of the turbine's transmission line. While multiple data channels are available, this study specifically emphasizes measurements obtained from channel 05, which is prominently highlighted within a dotted square on the generator diagram in Fig. 2. Moreover, the actual mounting configuration is depicted in Fig. 3, where it is evident that channel 05 is optimally positioned at the generator's input shaft, ensuring the shortest proximity to the monitored bearing among all installed accelerometers. Additionally, Fig. 4 illustrates the defects on the worn inner surface of rolling bearings, with red dotted areas marking inner race failures.

Wind turbine operations are inherently influenced by variable input rotational speeds, which arise from a combination of factors, including stochastic wind patterns, non-stationary load distributions, and dynamic transmission torques. Such variability poses a substantial challenge in developing reliable fault diagnosis protocols for operational wind turbine systems. Therefore, to establish consistent monitoring procedures while maintaining acceptable accuracy, it was necessary to analyze vibration measurements across a wide range of working conditions. However, particular attention was given to vibrations occurring at a typical rotational speed of 1080 r/min, as these conditions represent critical operational parameters.

The actual monitoring protocol was implemented under the following specified conditions:

- In accordance with the established monitoring schedule, data collection was conducted at semi-monthly intervals. The system employed a sampling frequency of 20,000 Hz, whereby 15 distinct data sets were collected at random intervals within each 24-h monitoring period for comprehensive analysis.
- 2. Given the inherent variability of meteorological conditions, achieving consistent rotational speeds of precisely 1080 r/min proved challenging. Therefore, to maintain the integrity of the health condition monitoring system, actual data collection dates occasionally deviated from the predetermined sampling intervals, though this was accounted for in the subsequent analysis.

4.1.2. Comparative analysis and results validation

The experimental analysis begins with a raw vibration signal, as illustrated in Fig. 5(a), which is inherently subjected to multiple forms of interference. These disturbances encompass diverse random external transient perturbations characterized by variable amplitudes across both high and low frequency spectra, while simultaneously being contaminated by environmental noise, predominantly of Gaussian nature. To facilitate a comprehensive and methodologically rigorous analysis of this complex vibration signal amid such noise conditions, it becomes imperative to implement sophisticated pre-processing techniques. In this context, the Discrete Wavelet Transform (DWT) emerges as a particularly suitable methodology, having demonstrated robust capabilities in signal decomposition while maintaining the integrity of intrinsic signal dynamics. Consequently, the level 1 approximation coefficient, which effectively encapsulates these preserved dynamic characteristics, is visualized in Fig. 5(b). Furthermore, the detailed coefficients at successive levels 1, 2, and 3, derived through systematic DWT implementation, are methodically presented in Fig. 5(c)–(e), respectively.

A comprehensive examination of the high-frequency components illustrated at each decomposition level reveals their exceptional capability to capture rapid signal variations, which frequently serve as critical early indicators of significant events in the signal's behavior. Conversely, the low-frequency components effectively demonstrate the fundamental structure and long-term evolutionary trends of the signal. The optimization of these coefficients through strategic application of low-pass filtering and threshold processing techniques proves crucial

for enhancing signal clarity and interpretation. This methodological approach effectively eliminates minor perturbations, substantially reduces noise artifacts, and simplifies the signal's complexity while maintaining its essential characteristics. Consequently, the long-term stability features of the signal become more prominently emphasized, and smallscale interferences are effectively suppressed, as evidenced in Fig. 5(f), (g). The reconstructed signal following wavelet transformation exhibits notable qualitative and quantitative advantages. Fig. 5(h) presents a comparative analysis between the original and reconstructed signals, demonstrating the significant impact of the implemented filtering and threshold processing techniques. The processed signal not only successfully eliminates unwanted noise but also enhances the distinctive features of significant external interferences, thereby improving the clarity of anomalous signal variations. Through this focused approach to core information extraction, the method substantially enhances both the precision and reliability of anomaly detection processes.

The methodology proceeds with a crucial signal processing step that involves partitioning the reconstructed signal into discrete states, as formally defined in Eqs. (15) and (16). In this process, the number of dynamically partitioned intervals is systematically varied between 10 and 20 to ensure comprehensive analysis. The resultant discrete signals demonstrate distinctly quantifiable distribution intervals under both standard operating conditions and noise-influenced scenarios, as comprehensively depicted in Fig. 6(a). Subsequently, building upon the equidistant discretization results, the derivatives of each transition frequency undergo rigorous statistical analysis to compute higher-order derivatives of the signal state distribution. This mathematical approach facilitates the identification and characterization of underlying transition patterns between signal states.

As evidenced in Fig. 6(b)-(g), the amplitude distribution of the discrete signals exhibits a pronounced concentration in the central interval, manifesting as a characteristic Gaussian-like distribution. The firstorder derivative's minimum value serves as a critical indicator, denoting the peak of signal transition frequency and thereby marking the crucial point where the proportion of normal states initiates its decline. Furthermore, through second-order derivative analysis, regions of decreased rate change in the first-order derivative are identified, thus indicating a significant deceleration in signal transition frequency reduction. Notably, the second local maximum of the second-order derivative demarcates the onset of this deceleration trend. Consequently, intervals occurring after this pivotal point are classified as abnormal, since their signal transition patterns demonstrate substantial deviation from established normal conditions. This comprehensive analysis enables the precise calculation of anomaly percentage indices for both normal fault source signals and abnormal interference source signals, thereby establishing essential parameters for subsequent peak rate threshold

Following the equidistant discretization process, two distinct heatmap visualizations are employed to elucidate the frequency and probability distributions of the Markov signals. Specifically, Fig. 7(a), presents the frequency heat-map of Markov signals, offering valuable insights into the regularity and patterns of state transitions within the Markov process. The pronounced diagonal elements indicate predominant stability in state patterns, while the bright off-diagonal elements reveal significant state transitions, thereby providing evidence of the system's inherent dynamics and potential anomalies.

A notable observation pertains to the presence of darker regions delineated by white boundaries, both along and distant from the diagonal. These white boundaries signify statistically infrequent or anomalous transition behaviors within the signal. The prominence of these boundaries serves as a quantitative indicator of the occurrence rate of these low-probability transitions. Subsequently, strategic adjustments to the heat-maps are implemented, including the systematic exclusion of self-transition frequency elements on the diagonal and the removal of high-frequency transitions off the diagonal. This refined process, accompanied by matrix normalization, results in a modified transition proba-

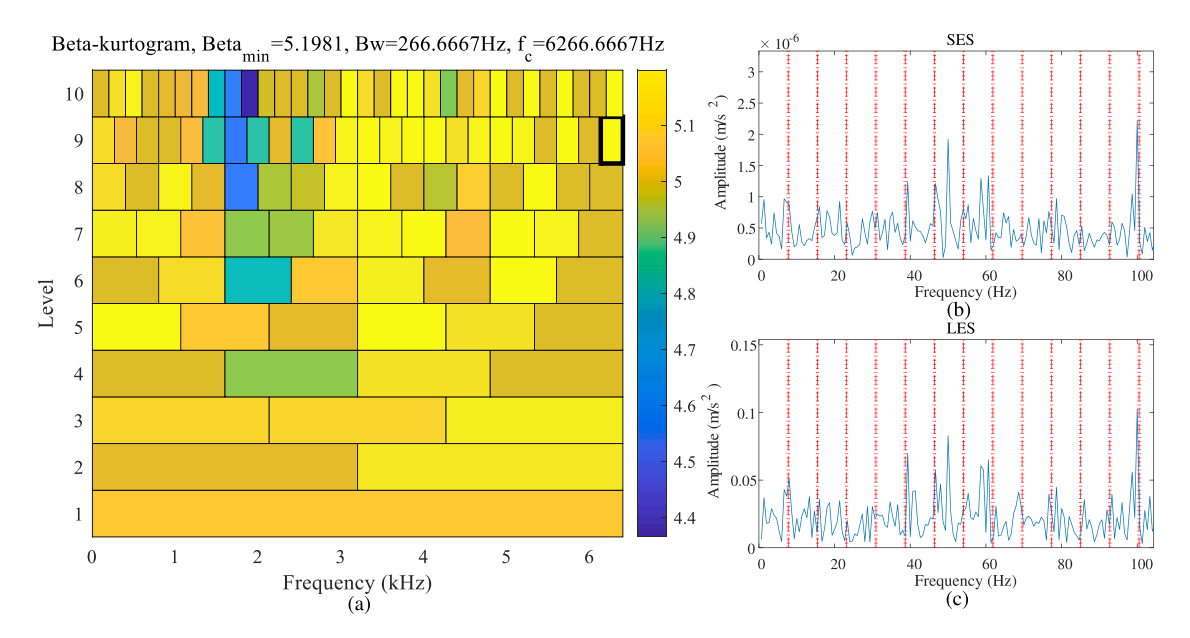


Fig. 28. Raw signal affected by external transient noise interference in Case II: (a) Demodulation band determination via Beta-Kurtogram, (b) Squared envelope spectrum, (c) Envelope spectrum in logarithmic scale.

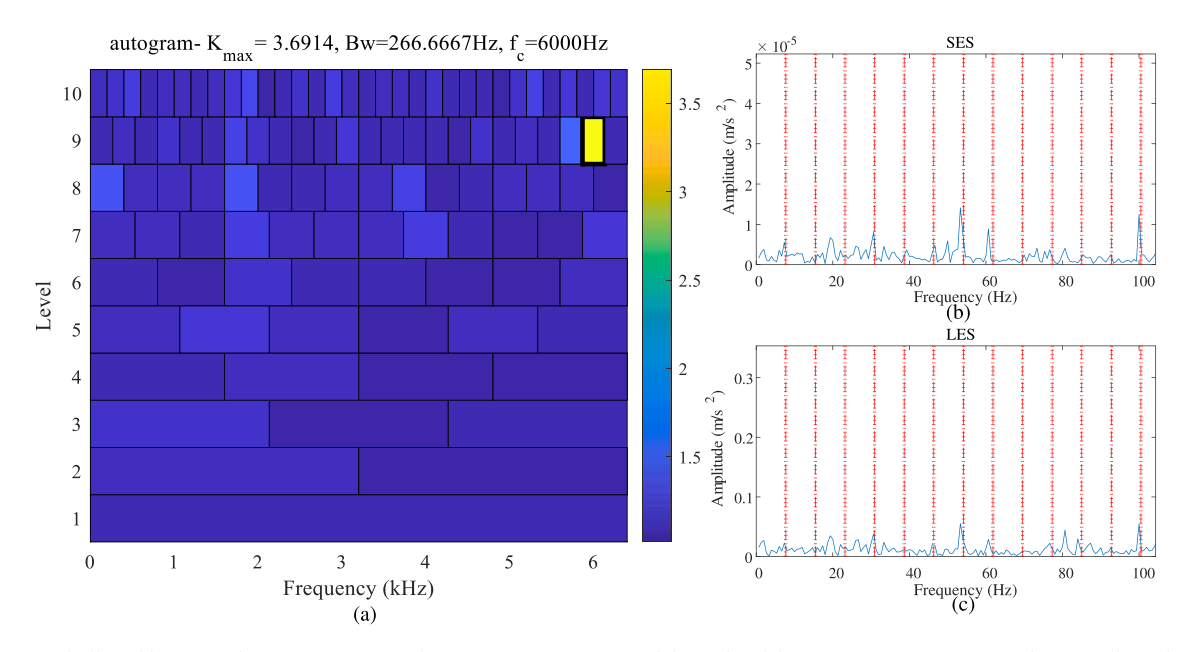


Fig. 29. Raw signal affected by external transient noise interference in Case II: (a) Demodulation band determination via Autogram, (b) Squared envelope spectrum, (c) Envelope spectrum in logarithmic scale.

bility matrix, as depicted in Fig. 7(b). These methodological adjustments effectively enhance the significance of lower-frequency transition elements, thereby expanding the dynamic range of the matrix and facilitating more nuanced identification of subtle changes or transition patterns that might otherwise remain obscured in the frequency matrix.

Subsequently, the mean of non-zero probabilities in the Markov transition probability matrix, calculated according to Eq. (23), is utilized as a crucial adjustment parameter in Eq. (17) to determine the anomaly percentage index. This index is systematically marked on the signal arranged in reverse order, as illustrated in Fig. 8. Through the application of Eq. (18), a significant red baseline emerges, effectively partitioning the sorted signal into two distinct regions. The adaptive peak rate threshold \hat{M}_d is then precisely determined

through the calculation of the differential means between these two regions.

To rigorously evaluate the efficacy of the proposed methodology in monitoring signal state transitions, comprehensive comparisons were conducted against several well-established techniques, including Short-Time Energy (STE) (Schirmer and Mporas, 2020), Short-Time Zero-Crossing Rate (STZCR) (Schirmer and Mporas, 2020; Chen et al., 2023a), and Short-Time Kurtosis (STK) (Alimi and Awodele, 2022). These comparative analyses are systematically presented in Fig. 9(b)–(f). The results demonstrate clear limitations in existing methods: the STZCR approach exhibits significant deficiencies in identifying transient noise interferences, as evidenced in Fig. 9(c), while the STE method merely highlights two high-energy spikes (Fig. 9(b)), with the overall signal remain-

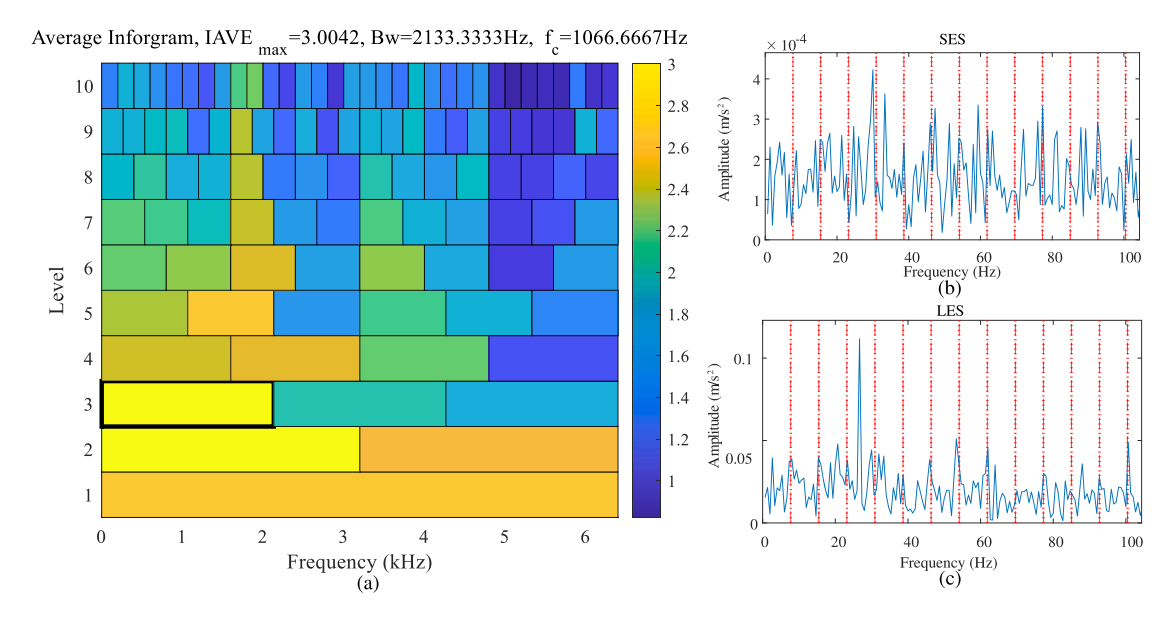


Fig. 30. Raw signal affected by external transient noise interference in Case II: (a) Demodulation band determination via Infogram, (b) Squared envelope spectrum, (c) Envelope spectrum in logarithmic scale.

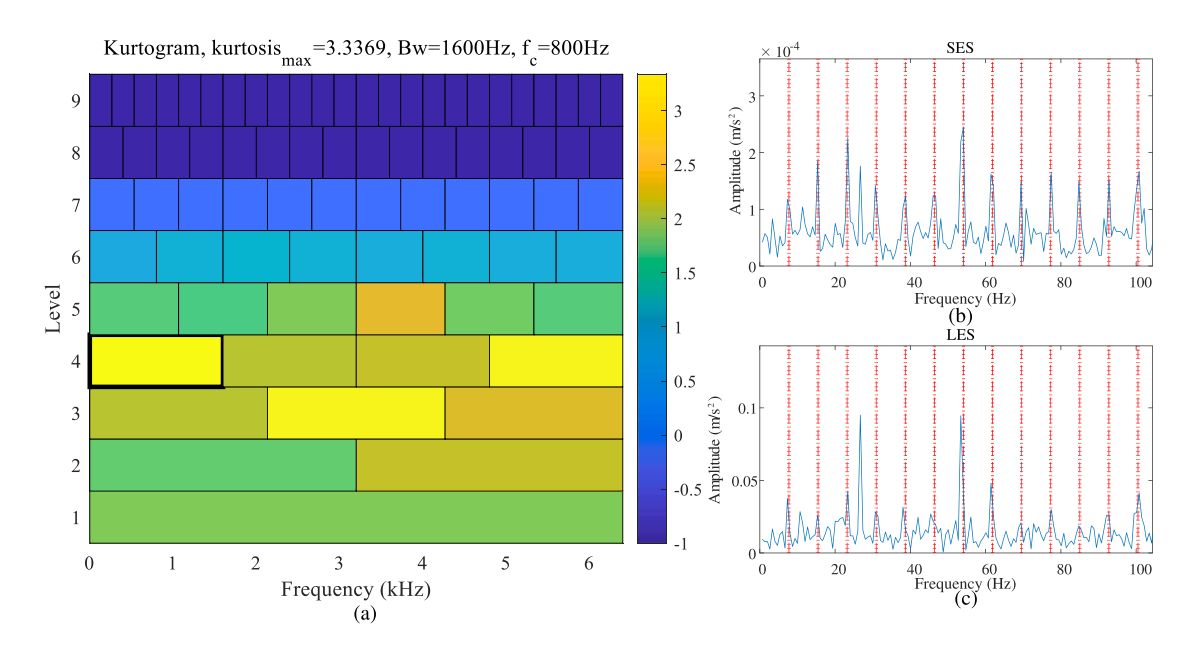


Fig. 31. Case II: (a) Fast-Kurtogram-assisted demodulation band selection for post-interference substitution and amplitude limitation, (b) Squared envelope spectrum, (c) Envelope spectrum in logarithmic scale.

ing notably cluttered. Although the STK method demonstrates relatively stable performance (Fig. 9(d)), it remains susceptible to significant noise from unrecorded signal components. In contrast, the Dynamic Markov Transition Frequency with Adaptive Peak Rates (DMTF-APR) method, illustrated in Fig. 9(e), exhibits superior performance characteristics, consistently and accurately detecting all transient noise interferences while maintaining robustness against other unknown signal distortions, thereby establishing itself as a more reliable and precise tool for signal state transition monitoring.

In accordance with Eqs. (26)–(29), a proposed approach involving the calculation of the period-weighted mean of key frequency domain components is implemented to replace anomalous signal fragments. This methodological enhancement serves the dual purpose of mitigating am-

plitude interference while preserving the intrinsic amplitude-frequency characteristics of the original time series, thereby substantially improving the reliability of fault diagnosis procedures. The efficacy of this disturbance suppression mechanism is comprehensively demonstrated in Fig. 10(a) and (b).

For comprehensive validation, the study employs multiple signal processing techniques—namely Fast-Kurtogram, Beta-kurogram, Autogram, and Infogram—in a comparative analytical framework. These methods are systematically applied to three distinct signal categories: original bearing vibration signals, signals exhibiting sensitivity to random transient noise interference, and post-interference replacement signals. The demodulation band selection results for untreated signals are meticulously documented in Figs. 11–14(a), "Demodulation Band Se-

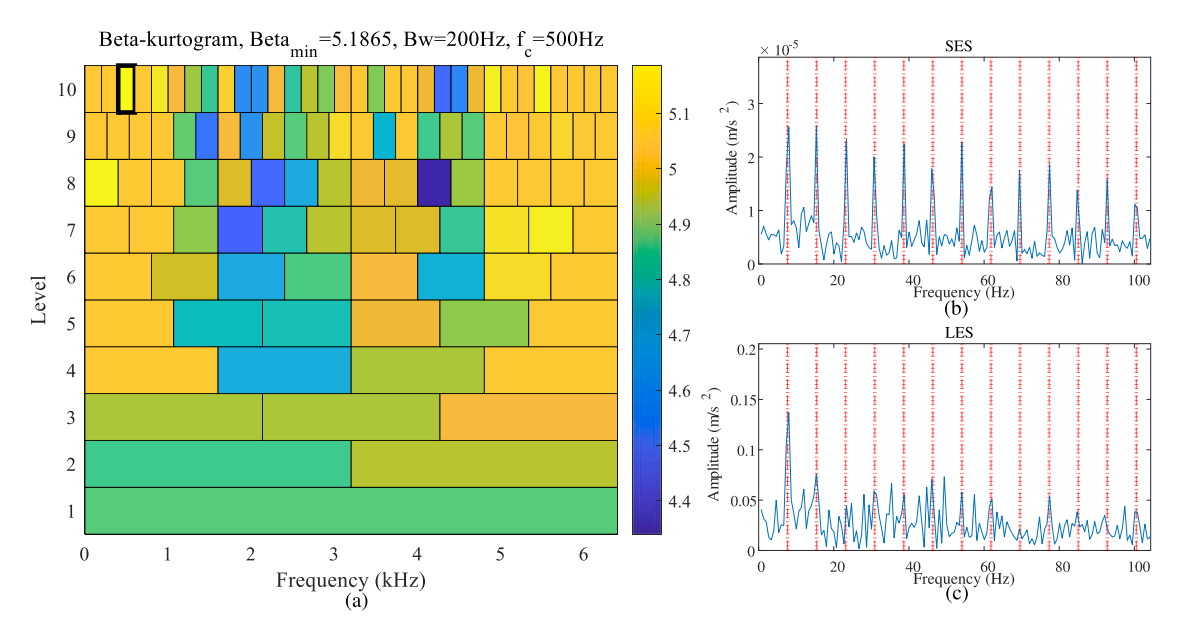


Fig. 32. Case II: (a) Beta-Kurtogram-assisted demodulation band selection for post-interference substitution and amplitude limitation, (b) Squared envelope spectrum, (c) Envelope spectrum in logarithmic scale.

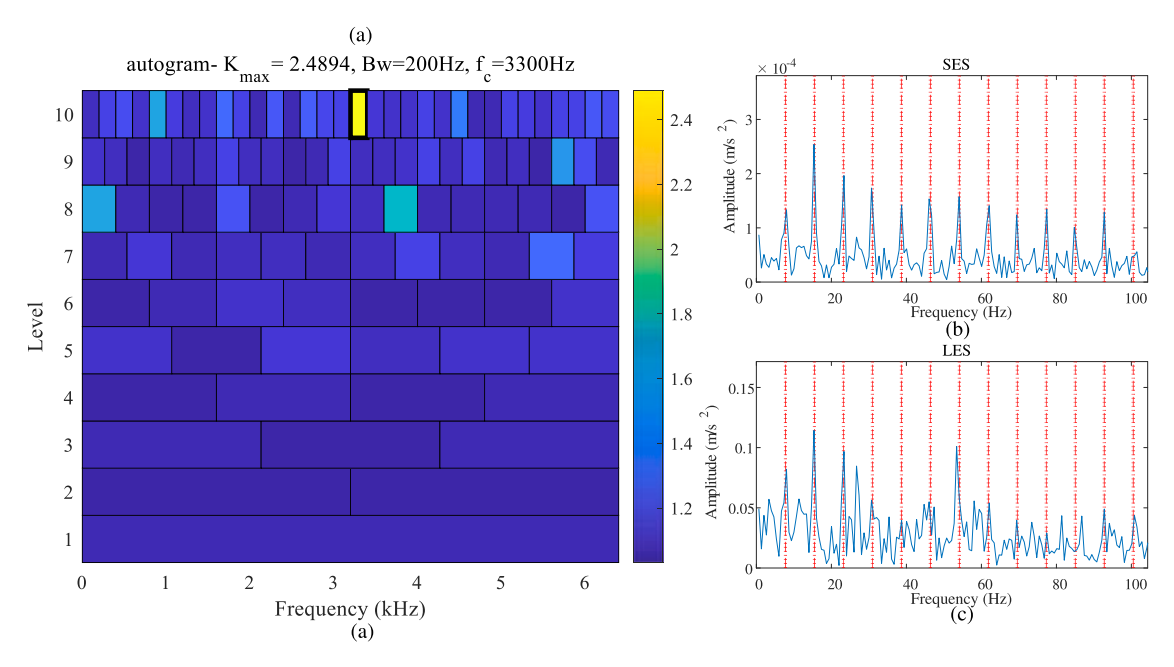


Fig. 33. Case II: (a) Autogram-assisted demodulation band selection for post-interference substitution and amplitude limitation, (b) Squared envelope spectrum, (c) Envelope spectrum in logarithmic scale.

lection Analysis." Subsequently, detailed envelope analyses utilizing both Squared Envelope Spectrum (SES) and Logarithmic Envelope Spectrum (LES) methodologies are presented in the corresponding (b) and (c) subfigures, yielding filtered central frequencies and bandwidths of [2500 Hz, 1250 Hz], [1500 Hz, 8750 Hz], [416.6667 Hz, 3541.6667 Hz], and [2500 Hz, 3750 Hz], respectively. However, a notable observation emerges from the envelope analyses: the absence of the theoretically calculated bearing characteristic frequency ($BPFI = 319.769 \, \text{Hz}$), indicating a potential limitation in the initial analysis approach.

The impact of implementing different demodulation bands and envelope analysis on post-interference suppression signals is extensively illustrated in Figs. 15–18. The optimized parameters for filtered central frequency and bandwidth are established as [5000 Hz, 2500 Hz], [1250 Hz, 1875 Hz], [1250 Hz, 6875 Hz], and [5000 Hz, 7500 Hz]. Significantly, the subsequent envelope analyses reveal distinct identifica-

tion of multiple characteristic frequencies (*BPFI*, 2*BPFI*, 3*BPFI*), thereby validating the robustness of the proposed methodological framework in addressing transitional states under conditions of transient non-Gaussian interference.

4.2. Case study II

4.2.1. Experimental configuration and data acquisition

The gearbox dataset, which serves as a comprehensive repository for fault diagnosis research, originates from a meticulously designed gear drive system that systematically encompasses multiple operating conditions and fault types. As illustrated in Fig. 19, the experimental apparatus comprises an integrated assembly of precision-engineered components, including a high-resolution tachometer, a variable-speed drive motor with precise control capabilities, a calibrated torque sensor for ac-

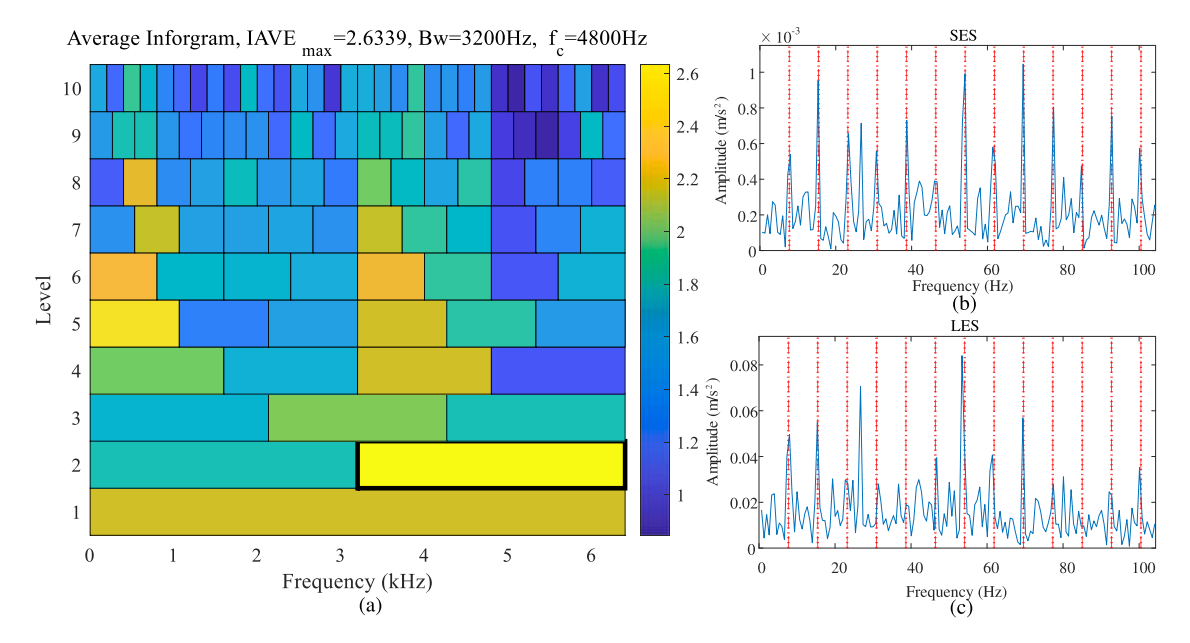


Fig. 34. Case II: (a) Infogram-assisted demodulation band selection for post-interference substitution and amplitude limitation, (b) Squared envelope spectrum, (c) Envelope spectrum in logarithmic scale.

curate measurement, a sophisticated two-stage parallel gearbox, a load gearbox, and a programmable load motor, all of which work synergistically to simulate authentic industrial operating conditions. Of particular significance is the strategic positioning of the accelerometer, which has been specifically mounted on an independent disk—a configuration that has been empirically determined to optimize vibration detection sensitivity and is depicted in enhanced detail in the magnified view of Fig. 19.

To ensure the capture of high-frequency transients and subtle system dynamics while maintaining signal fidelity, data acquisition is executed at a sampling frequency of 12.8 kHz, thus providing exceptional temporal resolution for comprehensive analysis. Moreover, to investigate the system's behavioral characteristics across diverse operational scenarios, the dataset encompasses an extensive spectrum of rotational speeds, which are methodically modulated between 1600 and 2400 r/min. Furthermore, the fundamental meshing architecture of the gears is precisely delineated in Fig. 20(a), while the comprehensive internal structural configuration of the parallel gearbox system is meticulously presented in Fig. 20(b), wherein the faulty gear component is distinctively demarcated with dotted lines to facilitate precise identification.

To establish a rigorous foundation for fault diagnosis analysis, vibration measurements are systematically acquired along the X-axis of the accelerometer while maintaining the gear at a predetermined operational speed of 1600 RPM. Each operational state, including the baseline healthy condition, comprises an extensive dataset of 768,000 discrete measurements, collected over a carefully controlled duration of 60 s. Consequently, this comprehensive and methodically constructed dataset serves as an invaluable resource for the development, validation, and refinement of fault diagnosis algorithms, thereby enabling researchers to conduct thorough investigations of various operational states and fault manifestations under rigorously controlled experimental conditions.

4.2.2. Comparative analysis and result validation

Fig. 21 illustrates the systematic decomposition and reconstruction process through DWT, encompassing the original signal characteristics, transformation procedures, and reconstructed outcomes. Upon examining Fig. 21(a), it becomes evident that the transient interference patterns within the gear fault signal manifest substantially more complex and stochastic characteristics compared to the bearing fault signal analyzed in Case 4.1. This heightened complexity consequently in-

creases the likelihood of misidentification between fault vibration components and interference patterns, potentially compromising diagnostic accuracy. Therefore, through the implementation of sophisticated preprocessing algorithms, extraneous background noise was systematically attenuated while preserving crucial transient interference and fault component characteristics, thereby establishing a robust foundation for subsequent fault identification protocols.

Fig. 22 presents the quantitative analysis of discretization outcomes across various equidistant intervals, incorporating both statistical sampling point distributions and dynamic multi-order differential analyses. The results demonstrate that the proposed second-largest value methodology effectively delineates the signal transition patterns from normal to high-interval values across different partition configurations, thereby establishing more precise boundaries between nominal and anomalous states.

The transition frequency matrix depicted in Fig. 23(a) reveals the comprehensive distribution of signal conversion patterns, with particular emphasis on the spatial concentration of normal self-transition behaviors along the diagonal region. This distribution pattern indicates that normal signal transitions predominantly occur within defined parametric boundaries, while subtle anomalous transitions, induced by stochastic disturbances, manifest in close proximity to the diagonal, establishing their contextual relationship with normal behavioral patterns. Furthermore, through the exclusion of normal transitional elements and subsequent normalization, as illustrated in Fig. 23(b), two distinct highlighted regions emerge along the diagonal, underscoring the statistical rarity of anomalous conversion probabilities within normal transition patterns.

The adaptive threshold, derived through the application of Eqs. (17) and 18, is visualized in Fig. 24. When applied to the modified peak rate and compared against conventional signal transition analysis methodologies (Fig. 25), the results conclusively demonstrate the enhanced capability of the proposed approach in identifying stochastic and uncertain interferences within complex operational environments.

Employing methodologies consistent with Case Study I, the Dynamic Markov Transition Frequency with Adaptive Peak Rates (DMTF-APR) indicator successfully identified and localized transient noise interferences. To preserve the integrity of amplitude-frequency characteristics, the framework incorporates an innovative mechanism replacing anomalous segments with normally weighted averages, thereby mitigating am-

P. Chen et al. Ocean Engineering 325 (2025) 120798

plitude interference effects and enhancing diagnostic reliability. As evidenced in Fig. 26, the seamless integration of replaced signals at original anomaly points validates the effectiveness of this approach.

In this case study, the comparative analysis employed benchmarking methods, specifically Fast-Kurtogram, Beta-Kurtogram, Autogram, and Infogram. The processed signals underwent a validation process, including the selection of demodulation bands and the execution of envelope analysis. The results of the demodulation band selection for the unprocessed signals can be observed in Figs. 27(a)-30(a). Subsequent envelope analysis utilized the Square Envelope Spectrum (SES) and Logarithmic Envelope Spectrum (LES), as shown in Figs. 27(b), (c), 28(b), (c), 29(b), (c), 30(b) and (c). These figures reveal the center frequencies and bandwidths determined by the selected methods, quantified as [2133.3333 Hz, 1066.6667 Hz], [266.6667 Hz, 6266.6667 Hz], [266 Hz, 8000 Hz] and [2133.3333 Hz, 1066.6667 Hz]. Upon closer inspection, the envelope analyses in Figs. 27(b), (c), 28(b), (c), 29(b), (c), 30(b) and (c) do not show the bearing characteristic frequency. This absence is noteworthy, particularly because it deviates from the theoretical calculation, which yields a characteristic frequency of $f = 7.73 \,\mathrm{Hz}$.

Following the identification and subsequent treatment of interferential elements through their replacement with weighted averages of normal segments, a second phase of analysis was conducted. The results of this refined analysis are presented in Figs. 31(a)-34(a), which collectively demonstrate the significant impact of utilizing different demodulation bands and implementing envelope analysis on the processed signal. Furthermore, Figs. 31(b), (c), 32(b), (c), 33(b), (c), 34(b), and (c) provide comprehensive results of the envelope analysis utilizing both SES and LES methodologies. In this refined analysis, the demodulation parameters, specifically the filter center frequencies and bandwidths, were precisely defined as [1600 Hz, 800 Hz], [200 Hz, 500 Hz], [200 Hz, 3300 Hz], and [3200 Hz, 4800 Hz]. Significantly, regardless of the specific demodulation band selection methodology employed, the results consistently demonstrated clear distinguish ability of multiple characteristic frequencies, including f, 2f, 3f, and their higher-order multiples. This robust outcome provides substantial validation for the effectiveness of the proposed Dynamic Markov Transition Frequency with Adaptive Peak Rates (DMTF-APR) method, particularly in complex operational environments and specifically in the context of diagnosing rotating equipment subject to random external interference.

5. Conclusion

This research presents a comprehensive methodological framework that effectively addresses the challenges of fault diagnosis in wind turbine bearing systems through the integration of adaptive signal tracking, dynamic Markov transition modeling, and enhanced noise suppression techniques. The framework makes several significant contributions: superior capability in capturing non-stationary fault signatures through adaptive signal tracking, effective characterization of complex fault patterns via dynamic Markov transition modeling, and successful minimization of transient interference noise through enhanced suppression techniques. Experimental results demonstrate significant performance improvements over existing approaches, particularly in challenging scenarios involving non-stationary signals and transient interference noise. Field testing has validated the framework's practical utility, showed improved early fault detection rates and reduced false alarms, which directly contribute to more efficient maintenance scheduling and reduced operational costs.

Building upon these achievements, several promising research directions have been identified for future work. First, researchers aim to integrate deep learning techniques for automated parameter optimization and real-time adaptation, while also investigating the framework's applicability to other renewable energy systems and industrial equipment. Moreover, the development of more efficient computational algorithms is essential for enhanced real-time processing capabilities, and

there are significant opportunities to explore integration with Industry 4.0 technologies such as IoT sensors and cloud-based monitoring systems.

Although this research has presented significant advancements, certain limitations persist that warrant further investigation. Specifically, researchers must address computational complexity to enable more efficient real-time processing, because the current system requires substantial computing resources. Furthermore, there is a need to reduce dependency on manual parameter tuning, and the framework's performance under extreme environmental conditions and in scenarios with limited fault data must be improved. Finally, broader validation across diverse turbine models and operational conditions is necessary to ensure long-term reliability and generalizability. Therefore, future efforts will focus on overcoming these challenges to further enhance the framework's robustness and practical applicability.

CRediT authorship contribution statement

Peng Chen: Writing – review & editing, Writing – original draft, Validation, Supervision, Resources, Project administration, Methodology, Investigation, Funding acquisition; Yuhao Wu: Writing – original draft, Visualization, Validation, Software, Resources, Methodology, Investigation, Data curation; Shuai Fan: Validation, Software, Resources, Methodology, Formal analysis, Data curation; Changbo He: Validation, Software, Resources, Funding acquisition, Conceptualization; Yaqiang Jin: Validation, Resources, Methodology, Investigation, Formal analysis; Junyu Qi: Validation, Software, Resources, Methodology, Investigation, Formal analysis; Chengning Zhou: Writing – original draft, Validation, Software, Resources, Methodology, Investigation, Formal analysis

Declaration of competing interest

The authors declare that they have no known competing financial interests or personal relationships that could have appeared to influence the work reported in this paper.

Acknowledgments

Partial funding for this research has been provided by several sources, including the National Natural Science Foundation of China through Grant 52105111 and 52305085, the Basic and Applied Basic Research Foundation of Guangdong Province through Grant 2022A1515010859, and the Shantou University (STU) Scientific Research Initiation Grant through Grant NTF21029, the Natural Science Foundation of Sichuan Province under Grant 2023NSFSC0861, the Nuclear Power Institute of China Original Foundation under Grant KJCX2022YC111, the China Postdoctoral Science Foundation under Grant 2023M740021, and the Natural Science Foundation of Anhui Province under Grant 2108085QE229.

References

Alimi, S., Awodele, O., 2022. Voice activity detection: fusion of time and frequency domain features with a SVM classifier. Comput. Eng. Intell. Syst 13 (3), 20–29.

Antoni, J., 2006. The spectral kurtosis: a useful tool for characterising non-stationary signals. Mech. Syst. Signal Process. 20 (2), 282–307.

Chen, B., Hu, Y., Wu, L., Li, H., 2023a. Partial discharge pulse extraction and interference suppression under repetitive pulse excitation using time-reassigned multisynchrosqueezing transform. IEEE Trans. Instrum. Meas. 72, 3535609.

Chen, P., Xu, C., Ma, Z., Jin, Y., 2023b. A mixed samples-driven methodology based on denoising diffusion probabilistic model for identifying damage in carbon fiber composite structures. IEEE Trans. Instrum. Meas. 72 (3513411), 1–11.

Chen, P., Li, Y., Wang, K., Zuo, M.J., 2020. A novel knowledge transfer network with fluctuating operational condition adaptation for bearing fault pattern recognition. Measurement 158, 107739.

Chen, P., Li, Y., Wang, K., Zuo, M.J., Heyns, P.S., Baggeröhr, S., 2021. A threshold self-setting condition monitoring scheme for wind turbine generator bearings based on deep convolutional generative adversarial networks. Measurement 167, 108234.

Chen, P., Wang, K., Zuo, M.J., Wei, D., 2019. An ameliorated synchroextracting transform based on upgraded local instantaneous frequency approximation. Measurement 148, 106953

P. Chen et al.

- Chen, P., Ma, Z., Xu, C., Jin, Y., Zhou, C., 2024a. Self-supervised transfer learning for remote wear evaluation in machine tool elements with imaging transmission attenuation. IEEE Internet Things J. 11, 23045–23054.
- Chen, P., Wu, Y., Xu, C., Jin, Y., Zhou, C., 2024b. Markov modeling of signal condition transitions for bearing diagnostics under external interference conditions. IEEE Trans. Instrum. Meas 73, 3518308.
- Chen, P., Wu, Y., Xu, C., Huang, C.-G., Zhang, M., Yuan, J., 2025. Interference suppression of nonstationary signals for bearing diagnosis under transient noise measurements. IEEE Trans. Reliab. (Early Access).
- Du, Y., Geng, X., Zhou, Q., Cheng, S., 2024. A fault diagnosis method for offshore wind turbine bearing based on adaptive deep echo state network and bidirectional long short term memory network in noisy environment. Ocean Eng. 312, 119101.
- Huang, C.-G., Huang, H.-Z., Li, Y.-F., Peng, W., 2021. A novel deep convolutional neural network-bootstrap integrated method for RUL prediction of rolling bearing. J. Manuf. Syst. 61, 757–772.
- Jia, M., Wang, J., Zhang, Z., Han, B., Bao, H., Wang, Y., 2024. Stakgram: a method for optimal demodulation band selection in bearing fault diagnosis under complex interference. Meas. Sci. Technol. 35 (12), 126134.
- Jin, Y., Xin, G., Antoni, J., 2023. Towards automated, integrated and unsupervised diagnosis of rolling element bearings. Mech. Syst. Signal Process. 203, 110691
- Kaewniam, P., Cao, M., Alkayem, N.F., Li, D., Manoach, E., 2022. Recent advances in damage detection of wind turbine blades: a state-of-the-art review. Renew. Sustain. Energy Rev. 167, 112723.
- Li, B., Xu, X., Tan, H., Shi, P., Qiao, Z., 2023. Cyclogram: an effective method for selecting frequency bands for fault diagnosis of rolling element bearings. Meas. Sci. Technol. 34 (9), 094003.
- Liu, D., Cui, L., Cheng, W., 2023. Fault diagnosis of wind turbines under nonstationary conditions based on a novel tacho-less generalized demodulation. Renew. Energy 206, 645–657.
- Maldonado-Correa, J., Torres-Cabrera, J., Martín-Martínez, S., Artigao, E., Gómez-Lázaro, E., 2024. Wind turbine fault detection based on the transformer model using SCADA data. Eng. Fail. Anal. 162, 108354.

- Panagiotopoulos, A., Dmitri, T., Spilios, F.D., 2023. Damage detection on the blade of an operating wind turbine via a single vibration sensor and statistical time series methods: exploring the performance limits of robust methods. Struct. Health Monit. 22 (1), 433–448.
- Peng, D., Zhu, X., Teng, W., Liu, Y., 2023. Use of generalized gaussian cyclostationarity for blind deconvolution and its application to bearing fault diagnosis under non-gaussian conditions. Mech. Syst. Signal Process. 196. 110351.
- Peng, J., Zhao, Y., Zhang, X., Wang, J., Wang, L., 2024. An adaptive reweighted-kurtogram for bearing fault diagnosis under strong external impulse noise. Struct. Health Monit. 23(6), 3336–3351.
- Schirmer, P.A., Mporas, I., 2020. Energy disaggregation from low sampling frequency measurements using multi-layer zero crossing rate. In: ICASSP 2020–2020 IEEE International Conference on Acoustics, Speech and Signal Processing (ICASSP). IEEE, pp. 3777–3781
- Sun, W., Zhao, X., Liu, D., Cui, L., 2025. Iesfsiogram: a novel adaptive method for optimal demodulation band determination in bearing fault diagnosis. Measurement 246, 116554.
- Wang, C., Qi, H., Hou, D., Han, D., Yang, J., 2024. Ensefgram: an optimal demodulation band selection method for the early fault diagnosis of high-speed train bearings. Mech. Syst. Signal Process. 213, 111346.
- Wang, H., Yan, C., Zhao, Y., Li, S., Meng, J., Wu, L., 2025. Seackgram: a targeted method of optimal demodulation-band selection for compound faults diagnosis of rolling bearing. Struct. Health Monit. 24 (1), 223–242.
- Xin, G., Zhong, Q., Jin, Y., Li, Z., Chen, Y., Li, Y.-F., Antoni, J., 2024. Autonomous bearing fault diagnosis based on fault-induced envelope spectrum and moving peaks-over-threshold approach. IEEE Trans. Instrum. Meas 73, 1–12.
- Yao, Y., Han, T., Yu, J., Xie, M., 2024. Uncertainty-aware deep learning for reliable health monitoring in safety-critical energy systems. Energy 291, 130419.
- Zemali, Z., Cherroun, L., Hadroug, N., Hafaifa, A., Iratni, A., Alshammari, O.S., Colak, I., 2023. Robust intelligent fault diagnosis strategy using kalman observers and neuro-fuzzy systems for a wind turbine benchmark. Renew. Energy 205, 873–898
- Zhang, K., Liu, Y., Zhang, L., Ma, C., Xu, Y., 2025. Frequency slice graph spectrum model and its application in bearing fault feature extraction. Mech. Syst. Signal Process. 226, 112383.
- Zhao, D., Wang, H., Cui, L., 2024. Frequency-chirprate synchrosqueezing-based scaling chirplet transform for wind turbine nonstationary fault feature time–frequency representation. Mech. Syst. Signal Process. 209, 111112.